

**Key Points:**

- Gravity, topography, and InSight seismic constraints are used to determine the average thickness of the crust of Mars
- The average thickness of the crust is between 30 and 72 km, and the maximum permissible crustal density is between 2,850 and 3,100 kg m⁻³
- The inferred crustal densities are compatible with a crust that is more felsic than typical Martian basaltic materials

Supporting Information:

Supporting Information may be found in the online version of this article.

Correspondence to:

M. A. Wiczeorek,
mark.wiczeorek@cnrs.fr

Citation:















Wiczeorek, M. A., Broquet, A., McLennan, S. M., Rivoldini, A., Golombek, M., Antonangeli, D., et al. (2022). InSight constraints on the global character of the Martian crust. *Journal of Geophysical Research: Planets*, 127, e2022JE007298. <https://doi.org/10.1029/2022JE007298>

Received 16 MAR 2022

Accepted 4 MAY 2022

Author Contributions:

Conceptualization: Mark A. Wiczeorek
Formal analysis: Mark A. Wiczeorek, Scott M. McLennan, Attilio Rivoldini, Catherine L. Johnson, Anna Mittelholz
Methodology: Mark A. Wiczeorek
Software: Mark A. Wiczeorek
Validation: Adrien Broquet
Writing – original draft: Mark A. Wiczeorek, Scott M. McLennan, Matthew Golombek, Caroline Beghein, Catherine L. Johnson, Doyeon Kim

Mark A. Wiczeorek¹ , Adrien Broquet² , Scott M. McLennan³ , Attilio Rivoldini⁴ , Matthew Golombek⁵ , Daniele Antonangeli⁶ , Caroline Beghein⁷ , Domenico Giardini⁸ , Tamara Gudkova⁹ , Szilárd Gyalay¹⁰ , Catherine L. Johnson^{11,12} , Rakshit Joshi¹³ , Doyeon Kim^{8,14} , Scott D. King¹⁵ , Brigitte Knapmeyer-Endrun¹⁶ , Philippe Lognonné¹⁷ , Chloé Michaut^{18,19} , Anna Mittelholz²⁰ , Francis Nimmo¹⁰ , Lujendra Ojha²¹ , Mark P. Panning⁵ , Ana-Catalina Plesa²² , Matthew A. Siegler¹² , Suzanne E. Smrekar⁵ , Tilman Spohn²² , and W. Bruce Banerdt⁵ 

¹Université Côte d'Azur, Observatoire de la Côte d'Azur, CNRS, Laboratoire Lagrange, Nice, France, ²Lunar and Planetary Laboratory, University of Arizona, Tucson, AZ, USA, ³Department of Geosciences, Stony Brook University, Stony Brook, NY, USA, ⁴Royal Observatory of Belgium, Bruxelles, Belgium, ⁵Jet Propulsion Laboratory, California Institute of Technology, Pasadena, CA, USA, ⁶Sorbonne Université, Muséum National d'Histoire Naturelle, UMR CNRS, Institut de Minéralogie, de Physique des Matériaux et de Cosmochimie, IMPMC, Paris, France, ⁷University of California Los Angeles, Los Angeles, CA, USA, ⁸Institute of Geophysics, ETH Zürich, Zürich, Switzerland, ⁹Schmidt Institute of Physics of the Earth RAS, Moscow, Russia, ¹⁰University of California, Santa Cruz, CA, USA, ¹¹The University of British Columbia, Vancouver, BC, Canada, ¹²Planetary Science Institute, Tucson, AZ, USA, ¹³Max-Planck-Institute for Solar System Research, Göttingen, Germany, ¹⁴Geology Department, University of Maryland, College Park, MD, USA, ¹⁵Department of Geosciences, Virginia Tech, Blacksburg, VA, USA, ¹⁶Bensberg Observatory, University of Cologne, Cologne, Germany, ¹⁷Université de Paris, Institut de Physique du Globe de Paris, CNRS, Paris, France, ¹⁸Ecole Normale Supérieure de Lyon, Université de Lyon, Université Claude Bernard Lyon 1, CNRS, Lyon, France, ¹⁹Institut Universitaire de France, Paris, France, ²⁰Harvard University, Cambridge, MA, USA, ²¹Rutgers University, Piscataway, NJ, USA, ²²German Aerospace Center (DLR), Berlin, Germany

Abstract Analyses of seismic data from the InSight mission have provided the first in situ constraints on the thickness of the crust of Mars. These crustal thickness constraints are currently limited to beneath the lander that is located in the northern lowlands, and we use gravity and topography data to construct global crustal thickness models that satisfy the seismic data. These models consider a range of possible mantle and core density profiles, a range of crustal densities, a low-density surface layer, and the possibility that the crustal density of the northern lowlands is greater than that of the southern highlands. Using the preferred InSight three-layer seismic model of the crust, the average crustal thickness of the planet is found to lie between 30 and 72 km. Depending on the choice of the upper mantle density, the maximum permissible density of the northern lowlands and southern highlands crust is constrained to be between 2,850 and 3,100 kg m⁻³. These crustal densities are lower than typical Martian basaltic materials and are consistent with a crust that is on average more felsic than the materials found at the surface. We argue that a substantial portion of the crust of Mars is a primary crust that formed during the initial differentiation of the planet. Various hypotheses for the origin of the observed intracrustal seismic layers are assessed, with our preferred interpretation including thick volcanic deposits, ejecta from the Utopia basin, porosity closure, and differentiation products of a Borealis impact melt sheet.

Plain Language Summary The crust, mantle and core are the three major geochemical layers that make up a planet. Before NASA's InSight mission, the thickness of the crust of Mars was inferred using indirect techniques, including analyses of gravity data collected from orbit and the composition of surface rocks. Estimates for the average thickness using these techniques spanned the range from 27 to 118 km. Analyses of data collected by the InSight seismometer have provided us with the first direct seismic measurement of the thickness of the crust, but this measurement is only for beneath the lander that is located in the northern lowlands where the crust is expected to be thinner than average. In this work, gravity and topography data are used to construct global crustal thickness models that satisfy the new seismic constraints. The average crustal thickness is found to be somewhere between 32 and 70 km, and the average density of the crust can be no larger than 3,100 kg m⁻³. This bulk crustal density is lower than most typical Martian

© 2022 The Authors.

This is an open access article under the terms of the [Creative Commons Attribution-NonCommercial License](https://creativecommons.org/licenses/by/4.0/), which permits use, distribution and reproduction in any medium, provided the original work is properly cited and is not used for commercial purposes.

Writing – review & editing: Adrien Broquet, Scott M. McLennan, Attilio Rivoldini, Matthew Golombek, Daniele Antonangeli, Caroline Beghein, Domenico Giardini, Tamara Gudkova, Szilárd Gyalay, Catherine L. Johnson, Rakshit Joshi, Doyeon Kim, Scott D. King, Brigitte Knapmeyer-Endrun, Philippe Lognonné, Chloé Michaut, Anna Mittelholz, Francis Nimmo, Lujendra Ojha, Mark P. Panning, Ana-Catalina Plesa, Matthew A. Siegler, Suzanne E. Smrekar, Tilman Spohn, W. Bruce Banerdt

basaltic materials, suggesting that the bulk composition of the crust is different from the volcanic materials at its surface.

1. Introduction

The crusts of the terrestrial planets record clues as to how these bodies formed and differentiated, how magmatic processes operated over billions of years, and how impact events modified and redistributed crustal materials (e.g., Taylor & McLennan, 2009). The most direct way to measure the thickness of the crust is by seismic means, which was first done for Earth by A. Mohorovičić using data from an earthquake in 1909 (see english translation in Mohorovičić, 1992). In addition to estimating the local thickness of the crust beneath a seismic station, seismic analyses also allow one to investigate layering of materials within the crust. Beyond Earth, seismic measurements have been made only on the surfaces of two planetary bodies: The Moon, as part of the Apollo program (for a review, see Lognonné & Johnson, 2015), and most recently Mars, as part of the NASA Interior Exploration using Seismic Investigations, Geodesy and Heat Transport (InSight) mission (Banerdt et al., 2020). Seismic measurements of crustal thickness are by nature sparse, so it is often necessary to use other data to extrapolate these when making maps or when determining quantities such as the average crustal thickness of the planet (e.g., van der Meijde et al., 2015; Wicczorek et al., 2013). In this work, we combine modeling of the gravity field of Mars with the new InSight seismic constraints to investigate the global character of the Martian crust.

Prior to NASA's InSight mission, several attempts had been made to estimate the average thickness of the crust of Mars and how it varies from place to place (see summary in Table 1). One common technique was to make use of gravity and topography data in combination with reasonable geologic assumptions. McGovern et al. (2002); McGovern et al. (2004) made use of a lithospheric flexure model to analyze the wavelength-dependent ratio of gravity and topography. Their analyses implied a best-fitting crustal thickness of about 50 km at three regions, but with acceptable values ranging from 8 to 68 km. Assuming that the crust of Mars was in a state of Airy isostasy, and by making use of a range of crustal densities, Wicczorek and Zuber (2004) used geoid-topography ratios over the southern highlands to estimate an average crustal thickness of 57 ± 24 km. Neumann et al. (2004) constructed a global crustal thickness map of the planet that satisfied the observed gravity field by explicitly assuming an average crustal thickness of 45 km. Baratoux et al. (2014), however, revisited their work and argued that the bulk composition of the crust was similar to that of the basaltic Shergottites, and was hence considerably more dense than assumed in that study. By assuming that the minimum thickness of the crust was close to zero, their analysis implied that the average thickness could be as large as 110 km. Lastly, using a localized spectral analysis of gravity and topography, Broquet and Wicczorek (2019) obtained local crustal thicknesses between 30 and 90 km for Pavonis Mons, Alba Mons, and Uranus Mons.

Several other techniques have been used to constrain the thickness of the Martian crust. Zuber et al. (2000), Nimmo and Stevenson (2001) and Guest and Smrekar (2005) noted that if the crust were sufficiently thick, high temperatures in the lower crust would give rise to enhanced rates of viscous deformation that would act to reduce lateral variations in crustal thickness. The observed surface topography across the Hellas impact basin and dichotomy boundary implied average thicknesses less than about 100 km. Global Martian geophysical data, such as the mean density, moment of inertia and tidal Love number are sensitive to the density profile of the planet, and these have been used in several studies that investigated the average crustal thickness, mantle properties, and core radius. These models are sensitive to the composition of the major geochemical reservoirs and the mantle temperature profile, and the study of Rivoldini et al. (2011) obtained a range of crustal thicknesses between 37 and 79 km (see also, Khan et al., 2018).

Given that the crust of Mars hosts a large fraction of the planet's heat producing elements (e.g., Taylor et al., 2006), its average thickness also plays an important role in the planet's thermal and magmatic evolution. By assuming a bulk abundance of heat producing elements of the planet, along with crustal abundances based on gamma ray spectroscopy measurements of the surface (Boynton et al., 2007), the crustal thickness directly impacts the present day heat flow, lithospheric thickness and the extent of present-day melting in the mantle (e.g., Hahn et al., 2011; Parro et al., 2017). When combined with elastic thickness constraints from the geologically young polar cap deposits (Broquet et al., 2020, 2021), these models favor average crustal thicknesses near 60 km, with allowable values between about 49 and 87 km (Plesa et al., 2018). Several studies have investigated other aspects concerning the global thickness and structure of the Martian crust, with a few notable examples including

Table 1
Selected Pre-InSight Crustal Thickness Estimates for Mars

Thickness (km)	Method	Reference
<100	Viscous relaxation of global shape	Zuber et al. (2000)
<115	Viscous relaxation of dichotomy boundary and Hellas impact basin	Nimmo and Stevenson (2001)
50 (26, 68)	Western rim of Hellas impact basin: Gravity-topography admittance	McGovern et al. (2002)
50 (8, 62)	Noachis Terra: Gravity-topography admittance	McGovern et al. (2002)
45	Global crustal thickness modeling	Neumann et al. (2004)
>29	Airy isostasy with minimum thickness equal to zero	Wieczorek and Zuber (2004)
57 ± 24	Isostatic geoid-topography ratios	Wieczorek and Zuber (2004)
<118	Thorium mass balance	Taylor et al. (2006)
37–79	Moment of inertia, Love number, thermodynamic modeling	Rivoldini et al. (2011)
27–110	Global crustal thickness modeling	Baratoux et al. (2014)
55–80	Moment of inertia, Love number, thermodynamic modeling	Khan et al. (2018)
49–87	Thermal evolution modeling with elastic thickness constraints	Plesa et al. (2018)
60 ± 20	Pavonis Mons: Gravity-topography admittance	Broquet and Wieczorek (2019)
50 ± 20	Alba Mons: Gravity-topography admittance	Broquet and Wieczorek (2019)
60 ± 30	Uranus Mons: Gravity-topography admittance	Broquet and Wieczorek (2019)

Note. Thicknesses are average values of the planet, unless otherwise specified. Values in parentheses represent 1- σ lower and upper limits.

Norman (1999), McLennan (2001), Sohl et al. (2005), Pauer and Breuer (2008), Cheung and King (2014), Tenzer et al. (2015), Ding et al. (2019), and Smrekar et al. (2019).

NASA's InSight mission landed on Mars on 26 November 2018 and deployed the first ever seismometer on the surface of this planet capable of recording a wide range of seismic activity (Banerdt et al., 2020; Lognonné et al., 2019). The prior seismometers carried by Viking 1 and 2 remained on the decks of those landers and were too strongly affected by meteorological phenomena (Anderson et al., 1977; Nakamura & Anderson, 1979). One of the primary objectives of the InSight mission was to determine the thickness of the crust beneath the lander, which is located in the northern lowlands between the Elysium rise and the dichotomy boundary. The initial analyses of the seismic data for crustal structure focused on using two different techniques for investigating converted and reflected seismic phases from layering beneath the lander (Knapmeyer-Endrun et al., 2021; Lognonné et al., 2020). The first technique was to compute seismic receiver functions, which removes the effects from the source and source-side structure on the seismic signal by a deconvolution technique. This method isolates precursor P phases and later S arrivals that were converted at layer interfaces (such as from S to P, or P to S). The second method used seismic interferometric techniques that made use of autocorrelations of both ambient noise and the codas of seismic events. For diffuse wavefields, the autocorrelations can be interpreted as vertical reflections from layers beneath the seismic station.

The receiver function analyses of Knapmeyer-Endrun et al. (2021) used the direct P wave from three major events and identified P-to-S converted phases that were consistent with either two or three crustal layers. Each crustal layer was treated as having a constant seismic velocity, and the velocity was found to increase abruptly at the interface of each layer. The first interface was at a depth of 8 ± 2 km, consistent with Lognonné et al. (2020), the second interface was at a depth of 20 ± 5 km, and the deepest, third interface was at a depth of 39 ± 8 km. The receiver function inversions of that study could not uniquely discriminate between the two- and three-layer crustal models because the direct converted phase from the deepest third interface arrived at nearly the same time as a reverberation in the uppermost layer. Distinguishing between these two models was complicated by the fact that all three seismic events had similar epicentral distances. In this same study, autocorrelation analyses, waveform modeling, and S-to-P converted phases from S receiver functions were used to support the existence of the first two layers, though they could not at that time conclusively resolve the deepest third layer (see also Kim, Davis, et al., 2021).

PP receiver function analyses were used by Kim, Lekić, et al. (2021) to test the above two- and three-layer seismic models of the crust. The benefit of using the PP ray for these analyses is that the distance to the bounce point is half that of the epicentral distance of the source. Though the converted phases from the third interface and the reverberation from the uppermost layer were coincident in time when using the direct P ray, these phases were predicted to be more separated when using the larger ray parameter of the PP ray. Synthetic receiver functions using a three-layer crustal model were shown to be more consistent with the observations than the two-layer model. This study also used S receiver functions to investigate P-wave precursors associated with the incident S wave. Unlike the P receiver functions, the P precursors arrive before any of the reverberations between layers. Consistent with the PP receiver functions, the S receiver functions also required a three-layer crust to fit the precursor phases. A re-analysis of the InSight seismic data by Durán et al. (2022) that included P receiver functions of seven events has also confirmed a three-layer structure with major seismic discontinuities in the depth ranges of 8–13 km, 22–27 km, and 37–47 km.

Even though the InSight seismic data have provided important constraints on the thickness of the crust beneath the InSight lander, these constraints are for a single location on Mars. Furthermore, the landing site is located in the northern lowlands, and the crustal thickness there is likely to be thinner than both the global average and that of the southern highlands (e.g., Neumann et al., 2004). In the initial analysis of Knapmeyer-Endrun et al. (2021), gravity and topography data were used to construct global crustal thickness models for the case where the density of the crust was everywhere the same. When combined with the InSight seismic thickness, it was possible to place tight constraints not only on the average thickness of the crust, but also on the maximum permissible density of the crust. In this study, we expand upon that work. We consider more complex density models of the crust, and we expand upon many of the details of the modeling, uncertainties, and implications. We present results for both the two-layer and three-layer seismic models, but based on the most recent analyses of Kim, Lekić, et al. (2021), we now have considerably more confidence that the thicker three-layer crustal model is the most probable of the two.

We first describe our methodology for constructing the global crustal thickness models from gravity, topography, and seismic constraints. The following three sections describe our model results using different assumed density structures of the crust. In the first, we describe our results for the scenario where the density of the crust is uniform. In the second, we discuss the implications of including a constant-thickness low density surface layer. In the third, we describe the results for the case where the northern lowlands crust is more dense than that of the southern highlands. In the discussion section that follows, we address several implications of our models. These include the implications of our average crustal thickness and crustal density constraints, the origin of crustal layering, and the origin and evolution of the crust. We conclude by discussing how further seismic constraints could improve our analyses. The mathematical details of our crustal thickness modeling are presented in an appendix.

2. Global Crustal Thickness Modeling

Our global crustal thickness modeling makes use of standard techniques that have been applied previously to the terrestrial planets and Moon (see Wiczorek & Phillips, 1998; Wiczorek et al., 2013, 2019). In its most general description, the observed gravity field is assumed to be the result of relief along the surface (which is usually known), relief along the crust-mantle interface, and the relief of hydrostatic density interfaces in the mantle and core. By making assumptions about the density structure of the crust, mantle and core, it is then possible to determine the relief along the crust-mantle interface that satisfies the observed gravity field. The crustal thickness is simply the difference in radius of the surface and crust-mantle interface, and the lateral variations in thickness are related to geologic processes such as impact cratering, extrusive volcanism, and intrusive magmatism.

In this work, we construct global models of the crust using both the two- and three-layer crustal thickness estimates beneath the InSight lander from Knapmeyer-Endrun et al. (2021), which are 20 ± 5 km and 39 ± 8 km, respectively. These values are largely consistent with the analysis of Durán et al. (2022), who obtained respective ranges of 22–27 and 37–47 km. In the following subsection, we first describe three different density models of the crust that we will consider in our modeling. We next describe conceptually the major aspects of modeling the gravity field of Mars, leaving the mathematical details to Appendix A. We then discuss some of the a priori input parameters of our models, and finally, we end with a short recipe that describes the relevant modeling steps. Preliminary versions of our crustal thickness models appeared in Smrekar et al. (2019), who summarized the

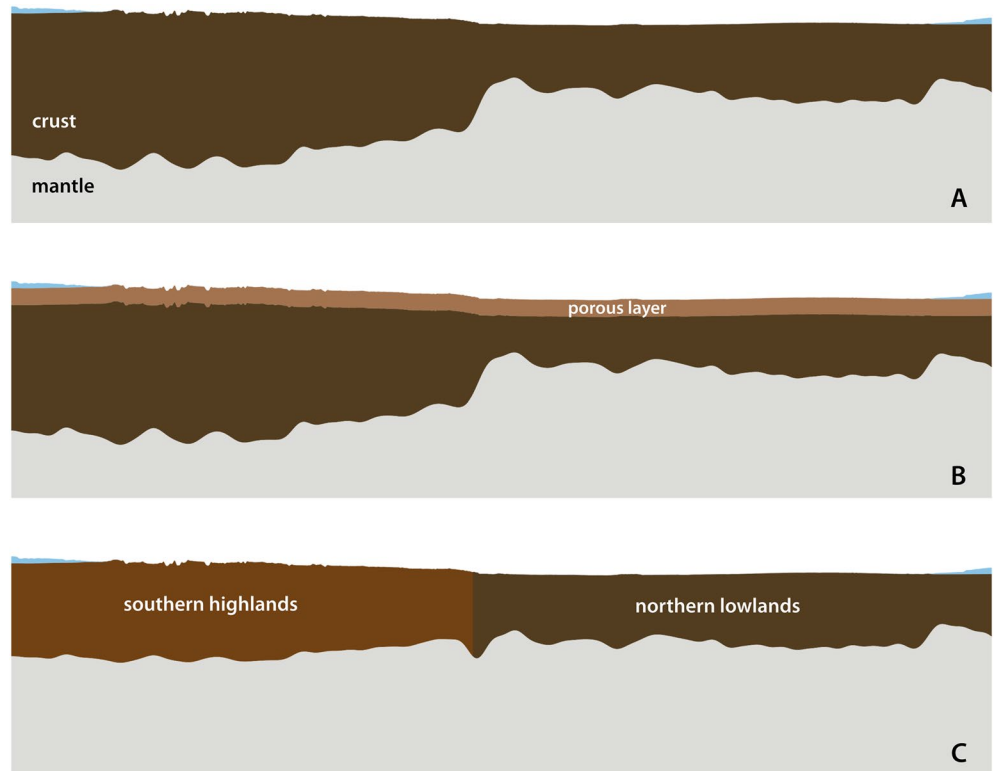


Figure 1. Three density models of the Martian crust used in the global crustal thickness inversions. The density of the crust is everywhere the same in model A (top), with the exception of the two polar ice caps that are shown in blue. Model B (middle) differs from model A in that it possesses an 8-km constant-thickness layer near the surface with a reduced density due to porosity. In model C (bottom), the density of the southern highlands crust is less than that of the northern lowlands crust. The surface topography and relief along the crust-mantle interface are shown for a pole-to-pole profile along 210° E longitude taken from the models presented in Figures 2 and 5. The InSight crustal thickness constraint lies in the northern lowlands, which is why the northern lowlands crustal thickness is similar in all three plots. The vertical exaggeration for each image is 20 times.

state-of-the-art knowledge of the Martian interior before InSight landed on Mars, and also in the work of Knapmeyer-Endrun et al. (2021) that made use of the first InSight crustal thickness constraints.

2.1. Density Models of the Crust

Our models depend directly on the assumed density structure of the crust. The crust of Mars is obviously complex in structure and heterogeneous in composition (e.g., Ehlmann & Edwards, 2014; McSween & McLennan, 2014; Nimmo & Tanaka, 2005; Pan et al., 2015; Sautter & Payre, 2021), but lacking detailed a priori knowledge about lateral and vertical variations in crustal density, it will be necessary to make simplifying assumptions that can be easily parameterized in our suite of inversions.

We consider three possible density models of the crust as illustrated in Figure 1. For the first model, we assume that the density of the crust is everywhere the same. The sole exception is that we take into account the low-density polar-cap deposits at both the north and south poles. Most of the previously published global crustal thickness models of Mars are broadly similar to this constant density model (e.g., Baratoux et al., 2014; Cheung & King, 2014; Neumann et al., 2004; Pauer & Breuer, 2008; Wieczorek et al., 2019). In our second model, we account for a constant thickness low-density layer at the surface of the crust. This layer could be the result of either porosity that closes at the same depth (e.g., Besserer et al., 2014) or a distinct compositional layer that is composed of aeolian, volcanic, impact, and/or sedimentary deposits. This low-density layer could extend either to the depth of the 8 or 20 km seismic discontinuity. For our last model, we consider that the density of the crust is different on either side of the dichotomy boundary as mapped by Andrews-Hanna et al. (2008). Motivated by the hypothesis that the dichotomy boundary could have been formed by a giant Borealis impact that would have

excavated the entire low-density crust and melted the underlying mantle (e.g., Andrews-Hanna et al., 2008; Marinova et al., 2008; Nimmo et al., 2008), our models will consider only the case where the density of the northern lowlands is greater than or equal to that of the southern highlands.

2.2. Gravity Field Modeling

The first step is to compute the gravitational attraction that arises from density interfaces beneath the rigid lithosphere of the planet. These interfaces are assumed to be in hydrostatic equilibrium beneath a depth of 150 km, which corresponds to the minimum present-day thickness of the elastic lithosphere beneath the south polar cap (Broquet et al., 2021). Unless otherwise specified, the lithosphere in this study will refer to that portion of the planet that can support deviatoric stresses over geologic time. The thermal lithosphere of Mars extends to a depth of about 450 km (Durán et al., 2022; Khan et al., 2021), but deviatoric stresses below the elastic lithosphere will relax over geologic time. For a given 1-dimensional density profile, the shapes of the hydrostatic interfaces are computed to conform to surfaces of constant gravitational potential using the technique developed in Wieczorek et al. (2019). This approach considers the presence of non-hydrostatic gravitational anomalies in the rigid lithosphere, and the relief along each hydrostatic interface is computed in order to be consistent with the observed gravitational field of the planet. The non-hydrostatic gravitational anomalies are a result of surface topography and mass anomalies placed at the average depth of the crust.

The shapes of the hydrostatic interfaces correspond primarily to flattened ellipsoids, with up to 2 km of additional long-wavelength relief that is similar in form to the geoid of Mars. As demonstrated in Wieczorek et al. (2019), for a wide range of interior density models, the sub-lithospheric mantle and core contribute only about 4%–6% to the degree-2 flattening term of the gravity field. Furthermore, they found that the additional gravitational signals related to the non-hydrostatic portion of the lithosphere affected subsequent global crustal thickness models only by about 2 km. Thus, the details concerning the calculation of the sub-lithospheric mantle and core gravity signals are expected to have only a minor effect on our final crustal thickness models.

The second step is to compute the gravitational attraction of the polar caps. For this, we use the MarsTopo2600 spherical harmonic model of the shape of Mars (Wieczorek, 2015) along with the bulk density and thickness maps of the two polar caps developed by Broquet et al. (2020); Broquet et al. (2021). These thickness maps were constructed to satisfy orbital radar constraints and account for the expected lithospheric flexure associated with the polar cap loads (see Appendix A). We note that if the low densities of the polar caps were neglected in our modeling, the crustal thickness beneath these deposits would be overestimated by about 10 km.

The third step is to compute the gravitational attraction associated with the surface relief of the crust with density ρ_c . For the crustal models that considered a constant-thickness reduced-density layer near the surface, the gravitational attraction of this layer was then subtracted from the topographic contribution using a density $\rho_c - \rho_\phi$, where ρ_ϕ is the bulk density of the layer. For crustal models that considered different densities north and south of the dichotomy boundary, it was necessary to compute the gravitational contribution of the surface relief using a modified finite-amplitude approach that was previously applied to the Moon (Wieczorek et al., 2013). For this latter case, it was also necessary to compute the gravitational attraction associated with these lateral density variations within a spherical shell bounded by the mean planetary radius and mean depth of the crust-mantle interface (see Appendix A).

The last step was to add up all of the gravitational signals that were computed above, and to subtract the result from the observed gravity field of Mars. For the observed gravity field, we made use of the model GMM3 (Genova et al., 2016) after truncating the spherical harmonic coefficients beyond degree 90 (which corresponds to the degree beyond which a regularization constraint was applied). The remaining signal was then assumed to be the result of relief along the crust-mantle interface, which was determined using an iterative numerical inversion technique that considered finite-amplitude effects (e.g., Wieczorek & Phillips, 1998; Wieczorek et al., 2013). For this last step, it was necessary to choose the average depth of the crust-mantle interface, and also to set the density of the uppermost mantle. For the mantle density, we made use of the uppermost mantle density from the 1-dimensional density profile used in the first step above, and assumed that this value was constant to the base of the lithospheric mantle at 150 km depth.

In order to stabilize the numerical inversions, and to reduce the effects of uncertainties in the gravity field that grow exponentially with depth, the numerical inversions made use of a minimum-amplitude downward

continuation filter that was constructed to possess a value of 0.5 at spherical harmonic degree 50. Though the choice of this filter is somewhat subjective, we note that the final models differed by only a few kilometers when using half-amplitude degrees between 40 and 60 (models using higher degrees have clear unrealistic oscillations related to noise in the gravity model). Given that this filtering step removes the shortest wavelength signal from the gravity model, the use of other gravity models with similar spatial resolutions, such as from Goossens et al. (2017) or Konopliv et al. (2020), would yield nearly identical inversion results. As described in Appendix A, we do not attempt to fit the total mass, moment-of-inertia, or tidal Love numbers of the planet.

2.3. Model Parameters

We consider the 1-dimensional density profiles of the mantle and core of Mars that were developed in Smrekar et al. (2019) and later expanded upon in Knapmeyer-Endrun et al. (2021). Our approach does not make use of the predicted density profile in the crust from these models, and the exact value of the core radius has little impact on our global crustal thickness models. We thus neglected a few models that differ only in how they treat the crust, and we chose that model whose core radius was closest to the InSight core radius of Stähler et al. (2021). Following the procedure described in Smrekar et al. (2019), we also constructed a model that is based on the best-fitting bulk silicate composition of Khan et al. (2022), the core radius of Stähler et al. (2021), and the temperature profile of Knapmeyer-Endrun et al. (2021). Unlike the other 1-dimensional models that assumed a bulk silicate composition based on Martian meteorite data, this model (henceforth referred to as Khan2022) was developed to satisfy the InSight seismic constraints with only limited cosmochemical assumptions. In total, we considered ten different density profiles. As will be demonstrated later, the most important aspect of these models is the density that they predict for the uppermost mantle.

After having chosen a 1-dimensional density profile for the mantle and core, it is necessary to assume a density for the crust. We assumed a minimum possible crustal density of $2,550 \text{ kg m}^{-3}$, and then considered all larger values that gave rise to physical solutions. Though this lower limit is somewhat arbitrary, it is a plausible value that is based on the bulk density of the lunar crust as measured by GRAIL (Wieczorek et al., 2013). The crust of the Moon is composed largely of the low-density mineral anorthite, and the more mafic crust of Mars would favor higher densities (see Baratoux et al., 2014; Belleguic et al., 2005, and Section 6.2). The crust of the Moon is also extensively fractured with about 12% porosity on average. Though the crust of Mars could also contain significant porosity, at least some portion of it would have been filled by ice, fluids, and/or aqueous alteration products. The higher temperatures and pressures on Mars would also have favored the viscous closure of pore space at shallower depths than on the Moon (Gyalay et al., 2020), which would tend to favor higher bulk crustal densities on Mars than the Moon.

We note that our chosen minimum density is compatible with an admittance analysis over the dichotomy boundary by Nimmo (2002) who obtained a best fitting density of $2,500 \text{ kg m}^{-3}$ for the upper crust. It is also compatible with an average crustal density of $2,582 \pm 209 \text{ kg m}^{-3}$ that was estimated by Goossens et al. (2017) using orbital gravity data. Though Goossens et al. (2017) reported densities as low as $1,800 \text{ kg m}^{-3}$ for extensive regions in the southern highlands, the lowest densities occurred where the spectral correlation between gravity and topography was the lowest, and where the uncertainties were the largest. Their localized analyses also did not consider the effect of lithospheric flexure, and this would act to bias their reported densities to lower values wherever the elastic thickness was low. They demonstrated that their models were consistent with density increasing with depth below the surface, so even if the low densities obtained by Nimmo (2002) and Goossens et al. (2017) could be representative of low-density surface deposits, the bulk density of the Martian crust, when averaged over all depths, is likely to be greater. Finally, we note that Lewis et al. (2019) obtained a relatively low density of $1,680 \pm 180 \text{ kg m}^{-3}$ for the central sedimentary deposits of Gale crater using in situ accelerometer data from the Curiosity rover and that Ojha and Lewis (2018) obtained a density of $1,765 \pm 105 \text{ kg m}^{-3}$ for the Medusae Fossae formation using orbital gravity data. Nevertheless, it is unlikely that these surficial deposits are representative of the deeper crust of Mars.

2.4. Modeling Summary

The main steps of the inversion can be summarized as follows: (a) Pick a 1-dimensional density profile to be used for the mantle and core beneath the elastic lithosphere, (b) pick densities to be used with one of the crustal

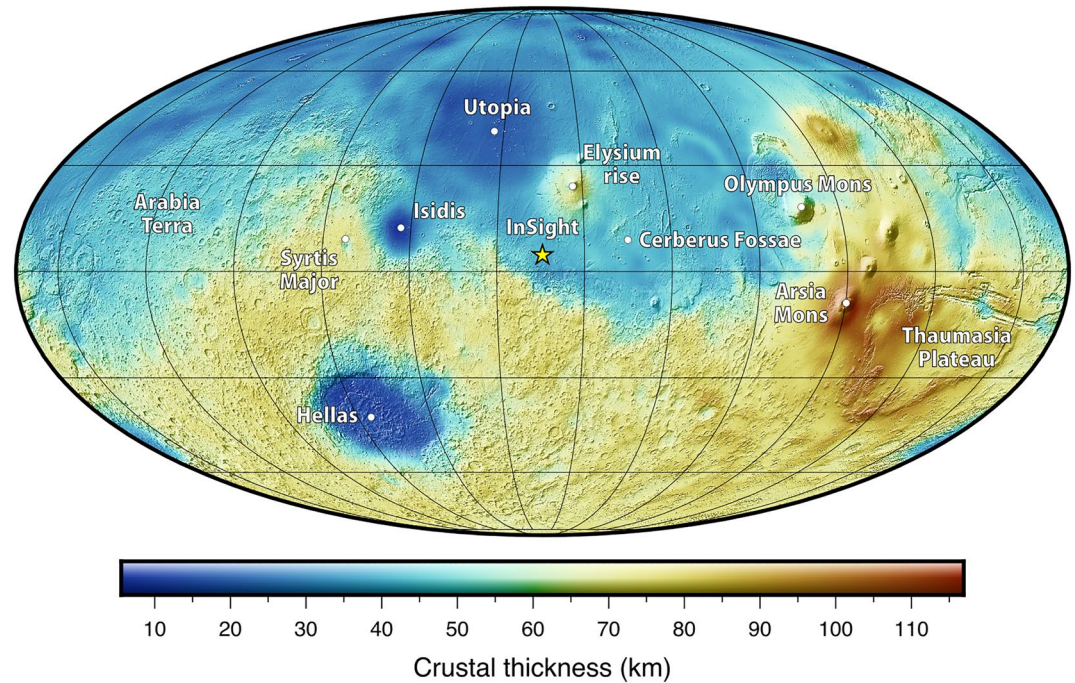


Figure 2. A global crustal thickness model of Mars with a uniform density crust (model A of Figure 1). For this specific model, the crustal density is everywhere $2,900 \text{ kg m}^{-3}$, the crustal thickness is constrained to be 39 km beneath the InSight lander (yellow star), and the mantle and core density is from the Khan2022 interior model. The average thickness of the crust is 57 km, the minimum thickness is 6 km in the interior of the Isidis impact basin, and the maximum thickness is 117 km in the southern region of the Tharsis plateau. To provide geologic context, the color intensities are modulated by a shaded-relief map derived from the surface topography. This map is presented in a Mollweide projection with a central meridian of 136° E longitude. Grid lines are drawn every 30° of latitude and longitude.

models in Figure 1, (c) pick an initial estimate for the average depth of the crust-mantle interface, (d) determine the relief along the crust-mantle interface using the methodology described above, and finally (e) compute the thickness of the crust at the InSight landing site. In order to obtain a specific thickness at the InSight landing site, it is only necessary to modify in an iterative manner the assumed average depth of the crust-mantle interface until the desired value is achieved. Once the desired thickness is obtained, one then needs to determine the minimum crustal thickness of the model to ensure that it is greater than zero. If the minimum value is negative, the set of input parameters should be excluded as being unphysical. All of these steps can be performed using the *ctplanet* software package (Wieczorek, 2021).

In the following three sections we discuss the results of our global crustal thickness modeling, first for the case of a constant density crust, second for the case with a low-density surface layer, and lastly for the case that considers a difference in crustal density across the dichotomy boundary.

3. Models With a Uniform Density Crust

A representative global crustal thickness model is presented in map form in Figure 2. For illustrative purposes, we use the Khan2022 density model for the mantle and core, we assume a crustal density of $2,900 \text{ kg m}^{-3}$, and we constrain the model to satisfy the best-fitting three-layer 39-km seismic thickness at the InSight landing site of Knapmeyer-Endrun et al. (2021). The location of the InSight lander is shown as the yellow star in this map, which demonstrates that it sits on representative crust of the northern lowlands, situated between the dichotomy boundary and Elysium volcanic rise. For a crustal thickness map that instead uses the 20-km seismic constraint, see Figure S1.

The features of this model are broadly similar to the model developed by Neumann et al. (2004). In particular, we note that the average thickness of the crust is 57 km. The minimum crustal thickness is about 5 km in the center of the Isidis impact basin, and similar, but slightly thicker values are found in the larger Hellas impact

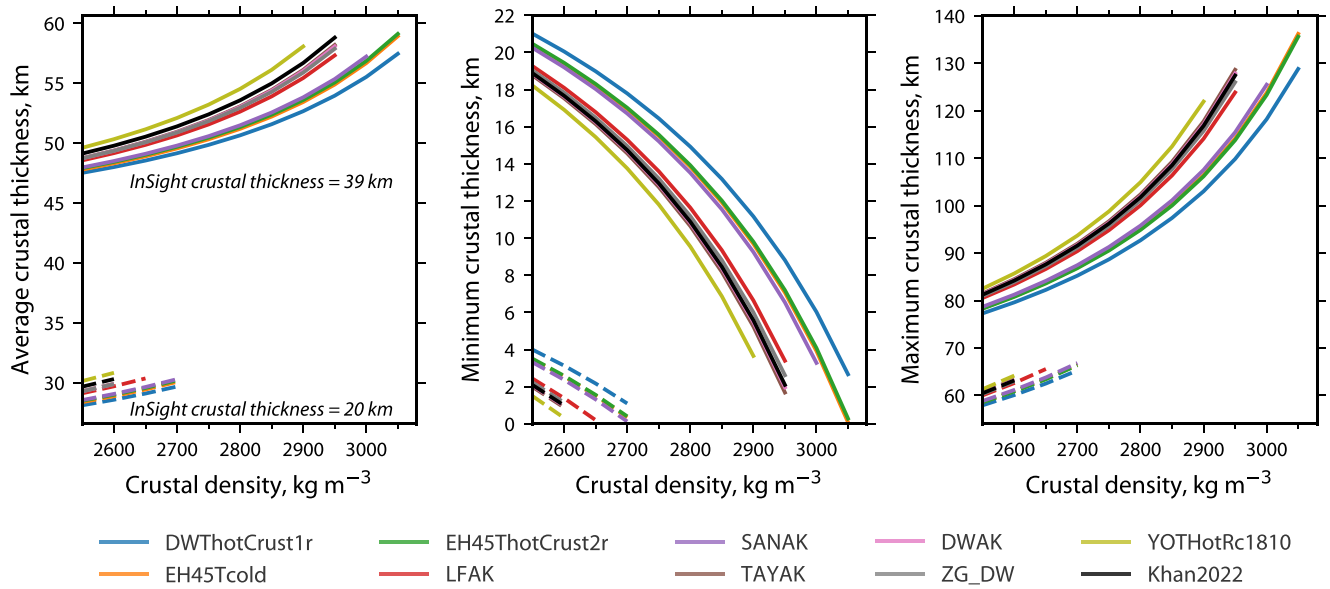


Figure 3. Summary of uniform-density crustal thickness models using a seismic constraint at the InSight landing site of either 39 km (solid lines) or 20 km (dashed lines). Average crustal thickness (left), minimum crustal thickness (center) and maximum crustal thickness (right) are plotted as a function of the assumed crustal density. Each colored curve corresponds to a different density model of the mantle and core as denoted in the legend. Note that because the crustal density of the models was discretized with an interval of 50 kg m^{-3} , the minimum thickness in the center panel never achieves exactly zero km: the density step after the last that is plotted would predict a negative thickness.

basin that is located in the southern highlands. The thickest crust is found in the southern portion of the Tharsis plateau, particularly in the region of Arsia Mons, and the Thaumasia highlands that are to the west and south of the Thaumasia Plateau. For this model, the maximum crustal thickness is just under 120 km. The transition across the dichotomy boundary from thick to thin crust is found to be abrupt for some regions (such as just south of the InSight landing site), whereas it is more gradual in other places (such as in Arabia Terra).

We summarize in Figure 3 how the assumed crustal density affects the average, the minimum, and the maximum thickness of our global crustal thickness models. Each colored curve corresponds to a different density model for the mantle and core, and we plot two groups of solutions: One group (solid lines) is constrained to satisfy the best-fitting seismic thickness of 39 km at the InSight landing site for the three layer crustal model, whereas the other group (dashed lines) is constrained to satisfy the best-fitting seismic thickness of 20 km for the two layer crustal model. The crustal density increases to the point that the minimum thickness of the crust is zero. Starting with the average crustal thickness plot, we see that the two possible seismic constraints lead to drastically different solutions. When using the 39-km seismic constraint, the average crustal thickness of Mars varies from a minimum of 48 km for the lowest crustal densities, up to 59 km for the highest densities. In contrast, for the 20-km seismic constraint, the average thickness is more tightly bound between 28 and 31 km.

In the center panel of Figure 3, the minimum crustal thickness of our models is seen to decrease as the density of the crust increases. This is because as crustal density increases, the difference in density across the crust-mantle interface decreases, and this requires an increase in relief along the crust-mantle interface to achieve the same gravity signal. The minimum crustal thickness is always found within the center of the Isidis impact basin, which is one of the rare lunar-like “mascon” basins on Mars (e.g., Ritzer & Hauck, 2009). When using the 39-km seismic constraint, the minimum thickness decreases from about 20 km for the lowest crustal densities to near zero at higher densities. The maximum permissible density for this model is about $3,050 \text{ kg m}^{-3}$. In contrast, when using the 20-km seismic constraint, the minimum thickness is always less than about 4 km, and the maximum permissible crustal density is considerably lower, only $2,700 \text{ kg m}^{-3}$. The rightmost panel in Figure 3 plots the corresponding maximum thickness of each model. We see that when using the 39-km seismic constraint, the maximum thickness is constrained to lie between 77 and 126 km, whereas for the 20-km seismic constraint, the maximum thickness is more tightly bound between 60 and 67 km.

Table 2

Summary of Constant Density Crustal Thickness Models Using Crustal Thickness Constraints at the InSight Landing Site of 39 ± 8 km and 20 ± 5 km for the 3- and 2-Layer Seismic Models, Respectively

Model	ρ_m , kg m ⁻³	3-layer seismic model		2-layer seismic model	
		Average thickness, km	Maximum ρ_c , kg m ⁻³	Average thickness, km	Maximum ρ_c , kg m ⁻³
DWThotCrust1r	3,493	39–68	2,950–3,100	24–37	2,550–2,850
EH45ThotCrust2r	3,462	40–70	2,950–3,100	25–40	2,550–2,850
EH45Tcold	3,459	40–70	2,950–3,100	25–38	2,550–2,850
SANAK	3,450	40–71	2,900–3,100	25–37	2,550–2,800
LFAK	3,400	40–71	2,900–3,050	27–37	2,550–2,750
ZG_DW	3,389	41–69	2,850–3,000	27–37	2,550–2,750
Khan2022	3,382	41–70	2,850–3,000	28–38	2,550–2,750
DWAK	3,380	41–69	2,850–3,000	27–37	2,550–2,750
TAYAK	3,376	41–69	2,850–3,000	27–37	2,550–2,700
YOTHotRc1810 km	3,352	41–72	2,850–3,000	29–38	2,550–2,700

Note. Ranges of values correspond to the 1- σ limits of the InSight seismic constraints. ρ_m is the density of the uppermost mantle just beneath the crust.

If the minimum thickness of the crust were known a priori, this would allow us to reduce somewhat our range of possible values for the crustal density and average crustal thickness. Though the minimum thickness of the crust could be close to zero in the center of the Isidis impact basin, as is the case with several impact basins on the Moon (Wieczorek et al., 2013), there is no reason that it could not be thicker. This could be the result of the impact event not having excavated all crustal materials in the center of the basin (e.g., Mancinelli et al., 2015), or from later infilling by lava flows and/or sedimentary deposits (e.g., Ivanov et al., 2012; Ritzler & Hauck, 2009; Searls et al., 2006). As an example, if it were known that there were 10 km of crustal materials present in the center of this basin, when using the 39-km InSight seismic constraint, the maximum permissible crustal density would be reduced somewhat from 3,050 kg m⁻³ to about 2,950 kg m⁻³. The upper limit of the average crustal thickness similarly would be reduced slightly from 59 to 53 km. Nevertheless, when using the 20-km seismic constraint, the minimum thickness for all our models is already less than about 4 km. Assuming any minimum thickness less than this would only affect the upper limit of the average thickness by no more than 3 km, and would reduce the maximum permissible density by no more than 150 kg m⁻³. Finally, we note that if the infilling material had a density that was substantially different than the surrounding crust, our predicted crustal thickness in the basin center could be biased by an amount that is comparable to the thickness of these deposits.

The models discussed above made use only of the best fitting seismic thickness at the InSight landing site for the two- and three-layer crustal models. As a result of the small number of suitable marsquakes that can be used to determine the crustal thickness, these numbers are uncertain by 5 and 8 km, respectively. We have created additional crustal thickness models using the entire range of the seismic constraints and summarize these results in Table 2 for each of the interior models. When considering the uncertainties associated with the three-layer seismic model, we find that the average crustal thickness is predicted to lie between 39 and 72 km, and that the maximum permissible bulk crustal density is 3,100 kg m⁻³. When considering the uncertainties associated with the two-layer seismic model, the average crustal thickness is predicted to lie between 24 and 38 km, with a maximum permissible bulk crustal density of 2,850 kg m⁻³.

The density that was used for the upper mantle, ρ_m , for each of the interior models is provided in Table 2, demonstrating that the maximum permissible crustal density increases as mantle density increases. The most important aspect of the density model used for the core and mantle is the density of the uppermost mantle, as this variable determines the magnitude of the relief along the crust-mantle interface that is required to satisfy the observed gravity field. To demonstrate this, we plot the average, minimum, and maximum crustal thickness in Figure 4 not as a function of crustal density, as was done previously, but as a function of the difference in density across the crust-mantle interface, $\rho_m - \rho_c$. Similar to Figure 3, we plot the model predictions for suites of solutions that

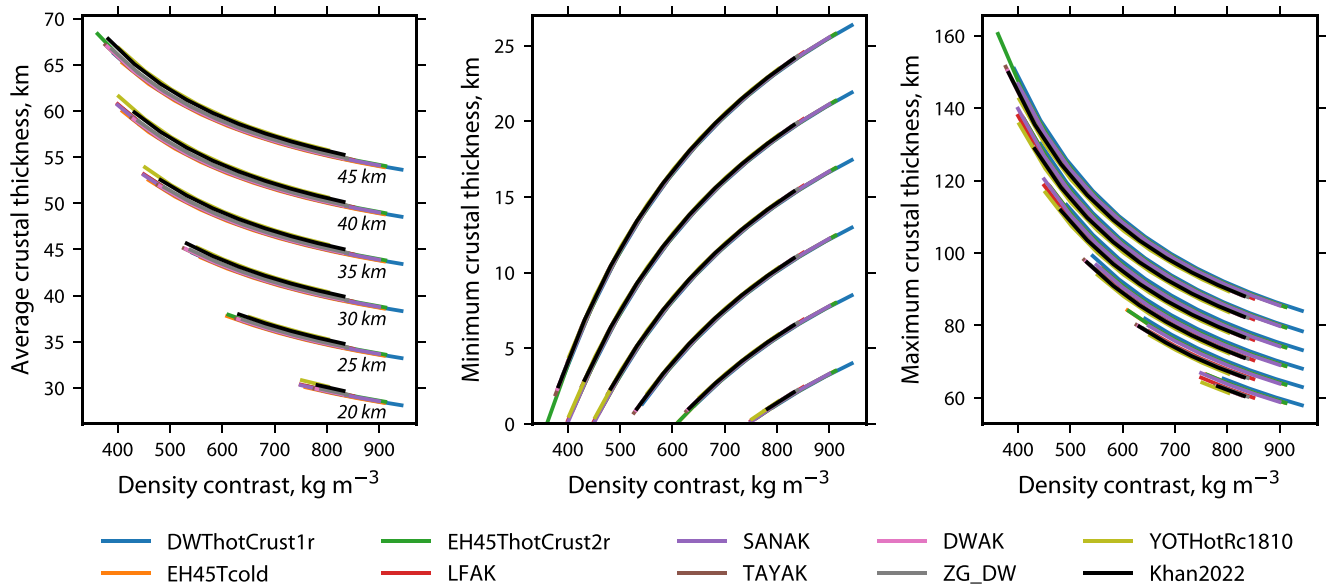


Figure 4. Summary of uniform-density crustal thickness models using different seismic constraints at the InSight landing site. Similar to Figure 3, each panel plots the average (left), minimum (center) and maximum (right) crustal thickness, but as a function of the difference in density across the crust-mantle interface ($\rho_m - \rho_c$). Each suite of tightly grouped curves uses a different seismic crustal thickness constraint beneath the InSight landing site, from 20 to 45 km. The density models of the mantle and core (colored curves) are the same as those in Figure 3.

satisfy a given crustal thickness at the InSight landing site, but for a larger range of values between 20 and 45 km. For a given thickness at the InSight lander, we see that the model predictions are nearly superposed. The average and minimum crustal thicknesses differ from each other by only a kilometer or two, with a little more variation existing for the maximum thickness curves. Though the curves are largely superposed, the limits of the plotted density contrasts differ for each given that each model has a different mantle density. This figure demonstrates that when parameterized in terms of the difference in density between the mantle and crust, the assumed density profile used for the mantle and core has little impact on the final crustal thickness models.

Lastly, we comment on one shortcoming of our constant density models. Gravity analyses have shown that many of the major volcanic edifices could have atypically high densities, up to about $3,300 \text{ kg m}^{-3}$ (e.g., Belleguic et al., 2005; Broquet & Wieczorek, 2019; McGovern et al., 2004). The densities of the volcanic constructs are comparable to those of the basaltic Martian meteorites (e.g., Baratoux et al., 2014), and are somewhat denser than what we obtain for the bulk density of the crust. One could attempt to account for the higher densities of these volcanoes, just as we did for the low-density polar deposits, but their densities and the corresponding amount of lithospheric flexure are considerably more uncertain than for the polar caps. The Tharsis province accounts for only 16% of the surface area of Mars, and the volcanoes cover an even smaller percentage of the Martian surface. Neglecting the expected higher than average densities of these regions will thus not have any significant impact on the average properties of our models. Nevertheless, we note that the thickness of the crust beneath these volcanic edifices will be biased to lower values in our models since we underestimate their contribution to the gravity field.

4. Models With a Low-Density Upper-Crustal Layer

We next consider the consequences of including a constant-thickness low-density layer that extends from the surface to an arbitrary depth d (model B of Figure 1). This layer could correspond to either one or both of the upper two crustal layers seen in the InSight seismic data, extending to either 8 or 20 km depth. We parameterize the density of this layer in terms of porosity ϕ , where $\rho_\phi = (1 - \phi)\rho_c$. In our modeling, we start with the same constant density crust model as used in the previous section, and to account for this layer, we simply subtract the gravitational contribution of a constant-thickness layer of density $\rho_c - \rho_\phi$. Whenever the low-density layer extends into the mantle, we account separately for the reduced mantle density $(1 - \phi)\rho_m$ in our calculations.

Since the relief of the top and bottom of this constant-thickness layer are the same, the gravitational contribution from the upper surface is nearly equal and opposite to that of the lower surface. The combined effect gives rise to lateral variations in gravity that are very modest, and that have little effect on our global crustal thickness models. The reduced density layer, however, does change the total mass of the crust, and this would hence have an impact on investigations of the moment of inertia of Mars.

As a demonstration, we consider the effect of adding a layer with a porosity of 15% and a thickness of 5, 10, and 20 km to the model displayed in Figure 2. For a deep crustal density of $2,900 \text{ kg m}^{-3}$, the density of the upper-crustal layer in this case would be $2,465 \text{ kg m}^{-3}$, which is comparable to the upper crustal density estimated by Nimmo (2002) and Goossens et al. (2017). We find that the average and maximum crustal thickness of the models with a porous layer change by less than 1 km, and that the minimum crustal thickness decreases by only 2 km for the model with the thickest layer. Somewhat larger crustal thickness differences up to 5 km were found to exist locally, but these are almost exclusively associated with Olympus Mons and the three Tharsis Montes.

Lastly, we note that crustal thickness models could be constructed that consider lateral variations in thickness of the upper crustal layer. Nevertheless, to do so, it would be necessary to either make explicit assumptions regarding the thickness of the upper layer, or to parameterize somehow its thickness in terms of the thickness of the others layers (e.g., Wieczorek & Phillips, 1998). At the present time, however, there are few constraints on how the thickness of the upper layer varies laterally. In fact, it is not even known if the three crustal layers beneath the InSight lander are global features of Mars, or if they just represent local geologic structures.

5. Models With a Dichotomy in Crustal Density

We next consider the consequences of having different crustal densities on either side of the dichotomy boundary. The most probable explanation for the origin of both the northern lowlands and dichotomy boundary is that they are the result of a giant Borealis impact event early in Martian history (e.g., Andrews-Hanna et al., 2008; Marinova et al., 2008; Nimmo et al., 2008). As this impact would have excavated the vast majority of pre-existing crustal materials, and would have also generated a thick impact melt pool that could potentially have differentiated to form a mafic crust (e.g., Vaughan & Head, 2014; Vaughan et al., 2013), we test the case where the density of the northern lowlands crust is greater than that of the southern highlands. For these models, we make use of the dichotomy boundary as mapped by Andrews-Hanna et al. (2008), acknowledging that certain portions of this boundary are somewhat uncertain, having been obscured by younger features such as the Tharsis plateau.

We plot a representative suite of models in Figure 5 that demonstrates the effect of reducing the density of the southern highlands crust with respect to the northern lowlands. The assumed crustal densities are plotted on the right, with the resulting crustal thickness model on the left. These models assume a 39 km thick crust at the InSight landing site, and make use of the Khan2022 density profile for the mantle and core. The uppermost model in this plot corresponds to the previously plotted model in Figure 2, where the density of the crust is everywhere equal to $2,900 \text{ kg m}^{-3}$. The three subsequent rows use the same density for the crust of the northern lowlands, but with densities of 2,800, 2,700, and $2,600 \text{ kg m}^{-3}$ for the southern highlands.

This suite of models has several notable features. The first is that the crustal thicknesses within the northern lowlands are nearly identical for all cases: This is because the density structure of the crust there is unchanged among the models, and also because the models are constrained to have the same thickness at the InSight landing site that is located within the northern lowlands. Second, as the density of the southern highlands decreases, the thickness of the crust there also decreases. Third, when the southern highlands are less dense than the northern lowlands by about 200 kg m^{-3} , there is no longer a prominent difference in the average thickness of the northern lowlands and southern highlands (see also Belleguic et al., 2005; Quesnel et al., 2009). This scenario is similar to that of Pratt isostasy, where variations in surface elevation are compensated by lateral variations in crustal density (cf. Watts, 2001). Lastly, whereas the thickest crust is located in the southern portion of the Tharsis plateau for the constant density model, the thickest crust is found in the northern portion of the Tharsis plateau when using the two lowest densities for the southern highlands. When the density of the southern highlands is about 100 kg m^{-3} less than that of the northern lowlands, the crustal thicknesses within the Tharsis plateau are broadly similar on either side of the dichotomy boundary.

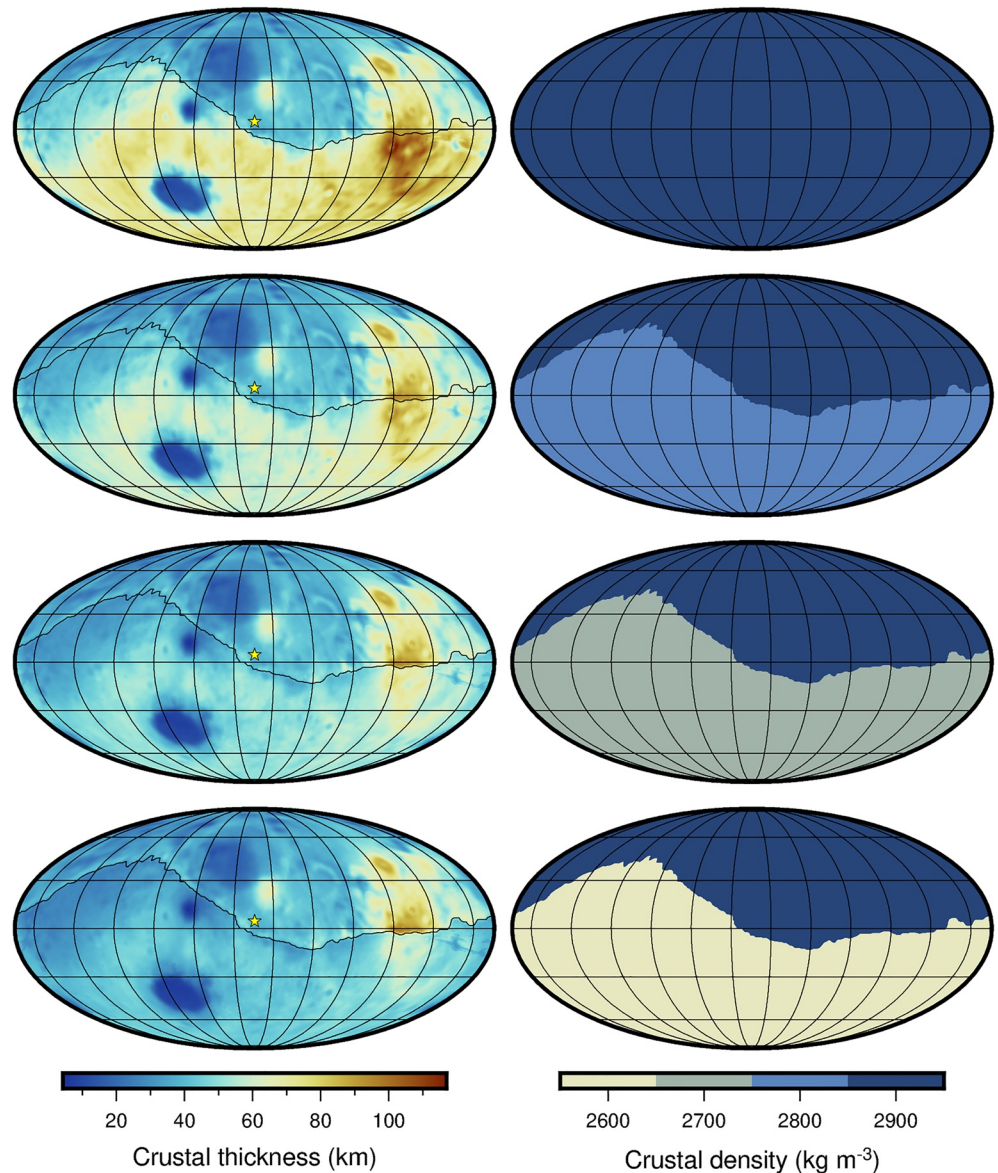


Figure 5. Global crustal thickness models that consider different densities north and south of the dichotomy boundary (model C of Figure 1). For this suite of models, the density of the northern lowlands is set to $2,900 \text{ kg m}^{-3}$, whereas the density of the southern highlands varies (from top to bottom) from $2,900$ to $2,600 \text{ kg m}^{-3}$ in 100 kg m^{-3} increments. For all models, the crustal thickness is constrained to be 39 km beneath the InSight lander, and the mantle and core density is from the Khan2022 interior model. The dichotomy boundary (black curve) is from Andrews-Hanna et al. (2008), and the uniform density model (top) is the same model as presented in Figure 2.

The average properties of the models that take into account a change in density across the dichotomy boundary are quantified in Figure 6. In these figures, we plot the average, minimum, and maximum thickness of the crust, similar to Figure 3. Each colored curve corresponds to a different density of the northern lowlands, ρ_{north} , and the curves are plotted as a function of the density of the southern highlands crust, ρ_{south} . The black curve corresponds to the case where the density of the northern lowlands is the same as that of the southern highlands, and is the same as the Khan2022 curve plotted in Figure 3. The models in this plot use the same Khan2022 interior model and InSight crustal thickness as in Figure 5.

We see that when the density of the southern highlands is less than that of the northern lowlands, the average thickness of the model is less than the model where the density of the crust is constant. This is simply a result of the fact that lower densities in the southern highlands reduces the crustal thickness there, giving rise to a lower

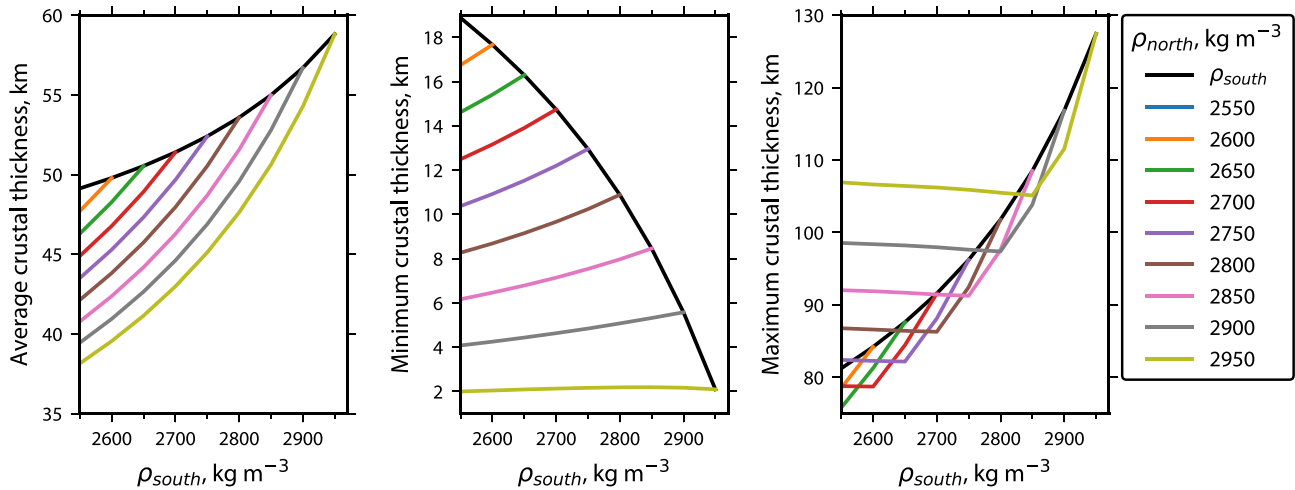


Figure 6. Summary of crustal thickness models that consider different crustal densities north and south of the dichotomy boundary. For this figure, only the Khan2022 density model of the mantle and core is considered, and the crustal thickness beneath the InSight landing site is assumed to be 39 km. Similar to Figure 3, each panel plots the average (left), minimum (center) and maximum (right) crustal thickness, but as a function of the density of the southern highlands, ρ_{south} . Each colored curve corresponds to a different assumed density of the northern lowlands, ρ_{north} , and the black curves correspond to the case where the densities of the northern lowlands and southern highlands are the same.

global average. Whereas the constant density model predicts average crustal thicknesses between 49 and 59 km, this suite of models predicts average thicknesses between 38 and 59 km. Neither the maximum permissible density nor the largest average thickness are modified with respect to the constant density model: only the lower bound of the average thickness decreases by 11 km.

The middle plot of Figure 6 shows that the minimum crustal thickness of our models is relatively unaffected by decreasing the density of the southern highlands crust. The minimum thickness decreases by only about 2 km for the lowest densities, and this behavior can be interpreted as being a result of two competing factors. First, as one decreases the density of the southern highlands crust, the average thickness decreases, which would act to decrease the minimum crustal thickness. But, second, decreasing the crustal density also increases the density contrast across the crust-mantle interface, and this acts to decrease the amplitude of relief along this interface, particularly within the Isidis impact basin. In the right panel of this plot, we see that the maximum thickness largely has the same behavior as the constant density model for large values of ρ_{south} . However, below a critical density, the maximum thickness switches from being in the southern to the northern portion of the Tharsis plateau. Decreasing ρ_{south} further beyond this point has little effect on the thickest crust that is now north of the dichotomy boundary.

Table 3
Summary of Crustal Thickness Models That Consider a Change in Density Across the Dichotomy Boundary

Model	Average crustal thickness, km	
	3-layer seismic model	2-layer seismic model
DWHotCrust1r	30–68	24–37
EH45HotCrust2r	32–70	25–40
EH45Tcold	31–70	25–38
SANAK	32–71	25–37
LFAK	33–71	27–37
ZG_DW	33–69	27–37
Khan2022	33–70	28–38
DWAK	33–69	27–37
TAYAK	34–69	27–37
YOTHotRc1810km	35–72	29–38

Note. The range of values correspond to using the 1- σ limits of the seismic thickness at the InSight landing site for the 3-layer (39 ± 8 km) and 2-layer (20 ± 5 km) crustal models. Note that the limits for the 2-layer seismic model are the same as for the constant density model.

The average crustal thickness results are summarized in Table 3 for each of the interior models used for the mantle and core, and for the range of crustal thickness constraints at the InSight landing site for the two- and three-layer seismic models. For the three-layer seismic model, the upper limit of the average value does not change with respect to the constant density models as summarized in Table 2: Only the lower limit decreases by about 10 km. When all models are combined, the range of the average crustal thickness is 39–72 km for the constant density crustal models, whereas for the models that consider lower densities in the southern highlands the range is 30–72 km.

For the thinner two-layer seismic model, the ranges of the average thickness do not change at all with respect to the constant density crustal models. The fact that the upper limits are unchanged is easily understood from Figure 6, but the reason that the lower limits do not change is somewhat different. To explain this behavior, we first note that none of the crustal thickness models

presented in this work can fit the InSight 1- σ lower limit for the two-layer seismic model of 15 km. Only one model can satisfy a thickness of 16 km at the InSight landing site, and additional models are progressively found as the seismic thickness increases. Nevertheless, as the seismic thickness increases, the first model that is found to satisfy the seismic constraint for each of our mantle and core density profiles corresponds to the case where the densities of the crust both north and south of the dichotomy boundary are 2,550 kg m⁻³. Thus, the lower limits for the two-layer seismic models are found to be the same as for our constant density models of the crust.

Lastly, we compute the total mass of the crust for the entire range of our successful models that consider different crustal densities north and south of the dichotomy boundary. When using the preferred three-layer seismic constraint, the total mass of the crust is found to be in the range 1.20–3.12 $\times 10^{22}$ kg. Using the best-fitting core radius of 1,830 km and a core density of 6,000 kg m⁻³ from Stähler et al. (2021), this corresponds to 2.5%–6.4% of the silicate mass of Mars. In contrast, if one were to use the thinner two-layer seismic constraint, the total mass of the crust would be 0.88–1.54 $\times 10^{22}$ kg, which corresponds to 1.8%–3.2% of the silicate mass of the planet.

6. Discussion

6.1. The Thickness of the Crust

The InSight landing site is located at low elevations in the northern hemisphere of Mars, and the crustal thickness at this locale is thus expected to be less than the global average of the planet. Nevertheless, this single point measurement provides a critical constraint to our global crustal thickness inversions that would otherwise be highly under-determined. For the most simple model that considers a uniform density crust, and for the entire range of possible interior models and crustal densities, the InSight seismic constraint of 39 ± 8 km implies that the average thickness of the crust should lie between 39 and 72 km. When considering a constant thickness low-density surface layer, the average crustal thickness of the planet was found to decrease only by about a kilometer. When considering crustal models where the density of the northern lowlands was greater than that of the southern highlands, the average thickness was constrained to lie between 30 and 72 km. In contrast, the 2-layer seismic constraint of 20 ± 5 km, which is no longer favored by the seismic data (Kim, Lekić et al., 2021), implies an average thickness between 24 and 40 km.

We note that these crustal thickness ranges are largely insensitive to the choice of the density profile used for the mantle and core. Though the interior model does influence the range of allowable crustal densities (as discussed in the following section), it does not affect the range of allowable crustal thicknesses by more than a few kilometers. The broad range of thicknesses that we obtain (from 30 to 72 km for the three-layer crustal model) is simply a combined result of the uncertainty on the InSight seismic constraint, which is 8 km, as well as our ignorance of the bulk crustal density. If the uncertainty on the seismic thickness could be eliminated, the range of average thicknesses would be reduced by about half (34–59 km for the best fitting seismic thickness of 39 km). Though it is unlikely that better a priori constraints on the bulk crustal density will be obtained, knowledge of the minimum crustal thickness in the center of the Isidis impact basin (such as from geological, tectonic, or perhaps magnetic constraints) could potentially be used to help reduce the range of allowable models.

The average thicknesses that we obtain are broadly consistent with those obtained in previous studies. For example, our range of 30–72 km is similar to the range of 33–81 km (1- σ limits) obtained by Wiczorek and Zuber (2004) using isostatic geoid-to-topography ratios. Neumann et al. (2004) assumed an average thickness of 45 km when constructing their global crustal thickness model that has since been widely used. Though this value is compatible with our study, our results are incompatible with the higher average thicknesses obtained by Baratoux et al. (2014), which were as high as 110 km. Our results are also broadly consistent with the range of 55–80 km obtained by Khan et al. (2018), who used moment-of-inertia and Love number constraints combined with thermodynamic phase stability calculations. Our results using the two-layer seismic constraint are not compatible with the range obtained by Khan et al. (2018) and are on the low end of the ranges obtained by modeling of the geoid and gravitational admittance.

In addition to the average crustal thickness of the planet, our models also constrain the magnitude of lateral variations in thickness across the planet. For illustrative purposes, predicted thicknesses at a few key locations and regions on Mars are provided in Table 4 for the uniform crustal density model that is displayed in Figure 2. We find that the crustal thickness beneath the InSight lander (39 km) is nearly equal to the average value of the northern lowlands when excluding the Tharsis province (37 km) (For the Tharsis province, we use a mask that

Table 4
Crustal Thicknesses at Key Localities and Regions on Mars

Region or location	Crustal thickness, km	
	Uniform density	$\rho_{\text{south}} = 2,700 \text{ kg m}^{-3}$
InSight landing site	39	39
Average	57	45
Cerberus Fossae ^a	44	44
Isidis impact basin	6	5
Hellas impact basin	12	9
Utopia impact basin	17	17
Argyre impact basin	30	22
Tharsis province	74	61
Southern highlands (excluding Tharsis)	63	44
South pole (excluding polar cap deposit thickness)	69	49
Northern lowlands (excluding Tharsis)	37	37
North pole (excluding polar cap deposit thickness)	30	30

Note. Values for the uniform density column are taken from the model presented in Figure 2 that makes use of the Khan2022 interior model, a crustal thickness at the InSight landing site of 39 km, and a uniform crustal density of $2,900 \text{ kg m}^{-3}$. Values in the last column correspond to the model presented in Figure 6 where the crustal density of the southern highlands is set to $2,700 \text{ kg m}^{-3}$. Impact basin crustal thicknesses are for the center of the basin.

^aCoordinates correspond to the locus of seismic events in this region at (8° N , 165° E).

corresponds approximately to the Amazonian, Hesperian, and late Hesperian volcanic geologic units AHv and IHv of Tanaka et al. (2014).) The crustal thickness at Cerberus Fossae, where the majority of currently identified seismic events are located (e.g., Giardini et al., 2021), is 44 km, which is only 5 km greater than the thickness at the InSight landing site. The average thickness of the southern highlands (when excluding Tharsis) is about 26 km thicker than the northern lowlands (63 versus. 37 km), and the average thickness of the Tharsis province is 11 km greater than that of the southern highlands (74 versus. 63 km). The thinnest crust is located within the Isidis impact basin with a thickness of 5 km, making it a prime candidate for having potentially excavated materials from the mantle of Mars (compare with Miljković et al., 2015, for the Moon). Lastly, we note that the thickness at the South Pole (excluding the polar cap deposits) is about 39 km greater than at the North Pole (69 versus. 30 km). This difference in crustal thickness has an important impact when interpreting the amount of lithospheric flexure associated with the polar deposits in terms of a subsurface temperature gradient (Broquet et al., 2020, 2021; Ojha et al., 2019, 2021; Plesa et al., 2018; Thiriet et al., 2018). As shown in Table 4, the differences in thickness between regions north and south of the dichotomy boundary are decreased when lower densities are considered for the southern highlands crust than for the northern lowlands. For these models, the dichotomy in crustal thickness is progressively replaced by a dichotomy in crustal density.

Lastly, we note that at sufficient pressure, crustal materials could have undergone a phase transition when they cooled, where plagioclase is converted to garnet. These rocks are referred to as granulites when plagioclase is still present in the host, and eclogites when all plagioclase has been exhausted. The density of garnet is significantly higher than the density of the upper mantle of Mars, so depending on its abundance, the bulk density of these rocks could have exceeded that of the underlying mantle. If this were to occur, they could potentially decouple geodynamically from the crust and recycle into the underlying mantle. In fact, it is conceivable that this phase transition could have provided a natural control on the maximum achievable crustal thickness of the planet (e.g., Baratoux et al., 2014). The depth at which crustal materials would have delaminated depends upon several factors, including the bulk composition of the crust, the temperature gradient, and the kinetics of the phase transition. For compositions similar to the basaltic Shergottites, Babeyko and Zharkov (2000) estimated that this should occur somewhere in the depth range of 60–120 km for their cold temperature profile that is similar to the temperature profiles predicted by Plesa et al. (2016). When considering the lowest upper mantle density used

in our modeling of $3,352 \text{ kg m}^{-3}$, their results predict that this transition could occur at even shallower depths, somewhere between 35 and 70 km.

Our models that use the 3-layer InSight seismic constraint predict maximum thicknesses between 77 and 136 km, opening the possibility that some form of limited crustal recycling could have occurred on Mars over its geologic evolution. Notably, when using the best-fitting seismic thickness of 39 km at the InSight landing site, our suite of models predicts average thicknesses within the Tharsis province between 57 and 80 km, with isolated values as high as 136 km. The average thickness of the southern highlands lies between 51 and 67 km, which could have allowed for crustal delamination under more restrictive conditions. In contrast, the average thickness of the northern lowlands lies between 35 and 39 km, implying that crustal delamination would never have occurred there. When considering the upper bound of the InSight 3-layer seismic constraint, the case for crustal delamination having occurred is only strengthened. In contrast, when using the 2-layer seismic constraint, crustal delamination could have occurred only in isolated regions within the Tharsis province and for only a limited set of our models.

6.2. The Bulk Density of the Crust

As one increases the density of the crust in our global crustal thickness inversions, the amplitude of the crust-mantle relief increases, and at some point the minimum thickness of the crust becomes zero. When this occurs, a firm constraint is obtained for the maximum permissible density of the crust. For each of our uniform density crustal models that make use of the $39 \pm 8 \text{ km}$ InSight seismic constraint, the maximum permissible density was found to be in the range of $2,850\text{--}3,100 \text{ kg m}^{-3}$. This range was unchanged when a constant thickness low-density surface layer was considered, or when lower densities were used for the crust of the southern highlands than the northern lowlands. In contrast, when considering the 2-layer seismic constraint of $20 \pm 5 \text{ km}$, which is no longer favored by the seismic data, we found that the maximum permissible density was between $2,550$ and $2,850 \text{ kg m}^{-3}$, where the lower limit is just the minimum value that we considered in our study. The permissible range of values for the maximum crustal density is a combined result of the uncertainty associated with the InSight seismic constraint, the range of densities that were used for the uppermost mantle, and our use of the most conservative constraint of having a minimum thickness of zero within the Isidis impact basin. If it were possible to improve our knowledge of any of these three factors, the maximum permissible density could potentially decrease, but would not increase. The inclusion of moment-of-inertia constraints could perhaps also reduce the range of allowable values (e.g., Knapmeyer-Endrun et al., 2021).

Our maximum permissible densities can be compared with results obtained from studies that modeled the wavelength-dependent relationship between gravity and topography for regions where there are large scale loads supported by the lithosphere (e.g., Belleguic et al., 2005; Beuthe et al., 2012; Broquet & Wieczorek, 2019; McGovern et al., 2004). These studies estimate the amount of lithospheric flexure for a given thickness of the elastic lithosphere, and then compare the predicted gravity with observations. Though these studies typically can constrain to good accuracy the density of volcanic edifices that are superposed on the crust, the density of the underlying crust itself is more difficult to constrain. Nevertheless, Broquet and Wieczorek (2019) were able to constrain both the density of the volcanic load and the underlying crust for three regions in the Tharsis province and two in the northern lowlands. The best-fitting crustal densities for these regions were $3,000\text{--}3,100 \text{ kg m}^{-3}$, with $1\text{-}\sigma$ limits between $2,880$ and $3,280 \text{ kg m}^{-3}$. A study by Pauer and Breuer (2008) obtained a compatible upper limit for the crustal density of $3,020 \pm 70 \text{ kg m}^{-3}$ based on global crustal thickness modeling and isostatic geoid modeling. These independent estimates are compatible with what we find, and imply that the density of the northern lowlands crust is probably close to our maximum permitted value of $3,100 \text{ kg m}^{-3}$. We emphasize that the maximum permissible density of $2,850 \text{ kg m}^{-3}$ that is obtained from using the 2-layer InSight seismic constraint is incompatible with these independent investigations of the Martian gravity field.

The range of maximum permissible bulk densities that we obtained for the crust is surprisingly low considering what is known about the average composition of Martian surface materials. Remote sensing data has shown that the surface of Mars is largely basaltic in composition (e.g., Ehlmann & Edwards, 2014; McSween et al., 2009), and because of the high FeO concentrations of these materials (e.g., Taylor et al., 2006) they are predicted to have grain densities that are considerably higher than those of terrestrial basalts. Using elemental abundances derived from gamma ray spectroscopy (which represent averages of the upper half meter of the surface over lateral distances of several hundred kilometers), Baratoux et al. (2014) estimated the grain densities of surface materials to be between $3,200$ and $3,450 \text{ kg m}^{-3}$ (see Table 5). They also reported similar densities for most igneous rocks at

Table 5
Grain Densities for Selected Igneous Compositions on Mars Computed From Estimated Normative Mineralogy

Lithology or geochemical reservoir	Grain density ^a , kg m ⁻³	Reference
Surface materials from GRS	3,200–3,450	Baratoux et al. (2014)
Basaltic and gabbroic Shergottite meteorites	3,060–3,420	20 samples compiled by Udry et al. (2020)
Average upper crust from soils	3,160	Taylor and McLennan (2009)
Gale crater gabbro norite (La_Reine)	3,140	Cousin et al. (2017)
Mars Pathfinder soil-free rock	2,970–3,020	Foley et al. (2003), Brückner et al. (2003)
Gale crater mugearite (Jake_M)	2,910	Stolper et al. (2013)
Gale crater trachybasalt endmember	2,830	Edwards et al. (2017)
Gale crater trachyandesite (Harrison C1)	2,790	Sautter et al. (2015)
Gale crater trachyte (Meeting_House)	2,750	Cousin et al. (2017)
NWA 7533 monzonite clast	2,680	Humayun et al. (2013)

^aGrain densities are computed using a CIPW mineralogic norm (Hollocher, 2022) with compositional data from the cited reference and assuming $Fe^{3+}/Fe_T = 0.10$. The density of the first entry was taken directly from Baratoux et al. (2014).

Gale crater, Gusev crater, and Meridiani Planum. Based on a compilation of 20 basaltic and gabbroic Shergottite meteorites (Udry et al., 2020), we find a range of densities between 3,060 and 3,420 kg m⁻³ for typical Amazonian magmatic rocks (see also Neumann et al., 2004). Lastly, based on in situ compositions of soils, Taylor and McLennan (2009) constructed an average composition of upper crustal materials on Mars that implies a grain density about about 3,160 kg m⁻³, which is also above our maximum permissible value.

One possible cause of the low bulk crustal densities that we obtain with respect to those of Martian basaltic materials is porosity. All of the terrestrial planets have been subjected to intense impact bombardment during the first ~600 My of their evolution, and these impacts would have, at least initially, fractured bedrock materials and deposited highly brecciated materials on the surface in their surrounding ejecta blankets. High resolution gravity data obtained for the Moon from the GRAIL mission imply a bulk density of 2,550 kg m⁻³ for the lunar crust, and when compared with estimated grain densities from remote sensing data, a porosity of about 12% was inferred (Wieczorek et al., 2013). Similar average porosities are found in shocked meteoritic materials and fractured bedrock beneath terrestrial impact craters, and it is not uncommon in both cases to find porosities that exceed 20% (see Consolmagno et al., 2008; Rae et al., 2019; Wahl et al., 2020, and references therein).

If we were to assume that the average grain density of the Martian crust was 3,300 kg m⁻³ then the introduction of a uniform lunar-like porosity of 12% would give rise to a bulk density near 2,900 kg m⁻³. Though this reduced density is compatible with our range of maximum permissible densities (2,850–3,100 kg m⁻³), there are good reasons to expect that crustal porosity would be less than this value on Mars, especially at depth. One way to reduce porosity at depth is by the viscous closure of pore space. Since viscosity is a strong function of temperature, modeling predicts that almost all porosity would be removed below a critical depth over a narrow interval of a few kilometers. Whereas the depth of pore closure was likely to be deeper than the crust-mantle interface on the Moon since ~4 Ga (Wieczorek et al., 2013), given the higher surface gravity and predicted heat flows on Mars, pore closure would have occurred at shallower depths on this planet. If the initial porosity was generated solely by impact bombardment during the first 600 My of Martian history, the model of Gyalay et al. (2020) predicts that all porosity should have since been removed from depths below about 12–23 km (for the case of a wet diabase rheology, a thermal conductivity of 1.5–2 W m⁻¹ K⁻¹, and a heat flow at that time of 60 mW m⁻²). The seismic discontinuity at 20 km depth beneath the InSight lander is therefore related potentially to a closure of pore space. Thus, while the upper portion of the Martian crust could perhaps exhibit lunar-like porosities (e.g., Goossens et al., 2017), it is unlikely that this porosity would persist to the base of the crust. In addition to pore closure, we might also expect somewhat reduced porosities on Mars with respect to the Moon, as some pore space would have been filled by ice, fluids, and aqueous alteration products (e.g., Borg & Drake, 2005).

Another explanation for the low crustal densities that we obtain is that the average crust of Mars could be more felsic than the basaltic materials found at the surface. Recent analyses of in situ compositional data from rovers, newly discovered meteorites, and orbital remote sensing data are now all pointing toward the possibility that

ancient feldspar-dominated and felsic rocks could be more widespread than once thought (for a review, see Sautter et al., 2016). For example, extremely feldspathic rocks, potentially anorthosites, have been detected at a few locations in the southern highlands using orbital near-infrared spectroscopy data (Carter & Poulet, 2013; Rogers & Nekvasil, 2015; Wray et al., 2013). Analyses of thermal emission spectroscopy data have detected evolved dacitic magmas in the summit region of Syrtis Major (Christensen et al., 2005). The average soil-free composition of five rocks analyzed at the Mars Pathfinder landing site, which are arguably igneous and derived from the southern highlands, have a composition that is between andesite and basalt-andesite (Brückner et al., 2003; Foley et al., 2003). Abundant alkali, felsic, and evolved magmatic rocks with Noachian ages (or older) have been identified at Gale crater with compositions including quart-diorite, granodiorite, and trachyandesite (Cousin et al., 2017; Sautter et al., 2015, 2016; Schmidt et al., 2014; Stolper et al., 2013). Analyses of the polymict breccia meteorite NWA 7034 and its pairings show that some igneous clasts have basaltic andesite, trachyandesite and even monzonite compositions (Humayun et al., 2013; Santos et al., 2015). And lastly, aqueous alteration of igneous rocks could account for some remote-sensing detections of quartz (Ehlmann et al., 2009; Michalski et al., 2021; Smith & Bandfield, 2012).

We estimate the grain densities for a few representative igneous rocks that have been analyzed in Gale crater and within the meteorite NWA 7533 (which is a pair of NWA 7034). Though the gabbro norite composition from Gale crater has a density of $3,140 \text{ kg m}^{-3}$, the more felsic compositions have densities that are considerably lower. The Mars Pathfinder soil-free rock has a density of about $3,000 \text{ kg m}^{-3}$, the felsic rocks in Gale crater are between $2,750$ and $2,910 \text{ kg m}^{-3}$, and the monzonite clast in NWA 7533 has a density of $2,650 \text{ kg m}^{-3}$. These evolved compositions could potentially make up an important volumetric component of the crust and could hence be a contributing factor to the low bulk densities that we obtain in this study. If this were the case, the small number of detections of these evolved compositions in the orbital remote sensing data could be explained by them having formed at depth as plutonic rocks, or having been hidden beneath a surficial layer of younger effusive basaltic lava flows, volcanic ash, aeolian deposits, and/or fluvial and lacustrine deposits. The fact that these compositions are rare in the Martian meteorite collection could simply be related to a sampling bias where it is easier to eject materials from impacts into competent materials than weak regolith materials (Head et al., 2002).

Lastly, the alteration of basaltic materials in the presence of water could perhaps contribute to lowering the bulk density of the crust. In particular, serpentinization is a process where the hydration of ultramafic to mafic materials such as olivine and pyroxene can be altered into serpentine and accessory minerals such as magnetite and brucite (e.g., Martin & Fyfe, 1970; Moody, 1976). As discussed in Toft et al. (2009) and Quesnel et al. (2009), the bulk density of the altered assemblage is generally lower than that of the unaltered materials. Nevertheless, the final density will depend upon many difficult to quantify factors, including the temperature gradient beneath the surface, how much water is available for the reactions, how much of the host rock is altered, the starting composition of the initial materials, and the proportions of the alteration products that are generated.

6.3. Origins of Crustal Layering

Analyses of the InSight seismic data indicate that there are three major seismic discontinuities beneath the lander where the seismic velocity abruptly increases. In addition to the crust-mantle interface at a depth of about 39 km, two intracrustal discontinuities are observed at depths near 8 and 20 km (Durán et al., 2022; Kim, Lekić, et al., 2021; Knapmeyer-Endrun et al., 2021; Lognonné et al., 2020). There are many possible explanations for the existence of large-scale layering within the crust, and most of these involve a change in crustal density. In this section, we assess several hypotheses using our improved knowledge of the thickness of the Martian crust and the density of typical Martian crustal materials. At the end of this section, we present one plausible interpretation of the three main crustal layers that are seen in the seismic data.

6.3.1. Constraints From Near Surface Stratigraphy

The InSight landing site is located in the northern lowlands of Mars, close to both the dichotomy boundary to the south and the Elysium volcanics to the north. The majority of the northern lowlands is covered by the Late Hesperian Vastitas Borealis formation that is widely believed to represent fluvial, lacustrine and/or marine sedimentary deposits (e.g., Tanaka et al., 2014). The InSight landing site, however, is located at slightly higher elevations in an older Early Hesperian transition unit (unit eHt; Tanaka et al., 2014) where the Vastitas Borealis formation is absent. This geologic unit is broadly parallel to the dichotomy boundary, being on average a couple

hundred km in width, though it is discontinuous in places and largely absent near the Tharsis province. In general, this unit is bordered to the north by a younger Late Hesperian transition unit (IHt) and to the south by an older Hesperian-Noachian transition unit (HNt).

Geologic mapping of the Early and Late Hesperian transition units near the InSight landing site strongly favors a volcanic origin for these two units (Golombek et al., 2017; Golombek et al., 2018; Warner et al., 2017; Pan et al., 2020). Mafic mineral detections in crater rims and central peaks, as well as rim-height measurements of partially embayed impact craters, imply that the extrusive lavas at the surface could extend to a depth of almost 0.2 km near the lander, and about 0.7 km elsewhere. Crustal materials beneath these basalts are in general mechanically weak based on the lack of rocks in the ejecta of large fresh craters in the broad plains surrounding the landing site (Golombek et al., 2017). These two observations are consistent with the existence of a high seismic velocity layer beneath the lander representing the basalts between depths of about 75–175 m, and lower velocities beneath this layer representing the mechanically weak materials (Hobiger et al., 2021). Layered deposits are present in the central peaks of six impact craters that formed in the Late Amazonian-Hesperian volcanic units to the northeast of the landing site. These deposits are likely to be sedimentary in origin and were excavated from depths of about 1–6 km below the surface. The central peaks of 20 other impact craters, however, do not show evidence for layered deposits, and many of these are located in the Early and Late Hesperian transition units, as well as the older Hesperian-Noachian transition unit that borders the dichotomy boundary. Sedimentary deposits hosting phyllosilicates have been detected at one locale in the Hesperian-Noachian transition unit close to the dichotomy boundary as well as within the central peak of a single impact crater that hosts layered deposits excavated from depths of about 6 km (Pan et al., 2020).

One interpretation of the upper crustal stratigraphy beneath the InSight lander is that the extrusive lavas at the surface are thin and extend only to a depth of about 0.2 km (see Golombek et al., 2017; Golombek et al., 2018; Hobiger et al., 2021; Pan et al., 2020; Warner et al., 2017). Beneath these lavas are mechanically weak sedimentary layered deposits, or perhaps pyroclastic deposits similar to the Medusae Fossae formation, some of which host phyllosilicates. Layered deposits are known to be present at depths up to 6 km below the surface within the adjacent Late Amazonian-Hesperian volcanic units, and it is conceivable that these deposits could extend laterally beneath the InSight lander, perhaps all the way to the dichotomy boundary (Pan et al., 2020). These layered deposits could extend to the base of the upper crustal layer at 8 km depth, and could account for the low seismic velocities of this layer.

An alternative interpretation is that the extrusive lavas at the surface extend all the way to the base of the upper crustal layer at 8 km depth. In this scenario, the lava flow thicknesses obtained from embayed craters would represent only the thickness of lavas that erupted since the crater formed, and not the total thickness that would include lavas older than the impact event. The sedimentary deposits detected in the central peaks of six impact craters would represent isolated deposits, given that 20 similarly sized craters in the surroundings show no evidence for buried sedimentary deposits. To account for the low seismic velocities of the upper 8 km of the crust, these volcanic deposits would need to be highly fractured, plausibly as a result of high impact rates in the Noachian, and/or to have undergone substantial aqueous alteration (Lognonné et al., 2020).

6.3.2. Depth Variations in Porosity

The addition of porosity to a rock can dramatically reduce its seismic velocity (e.g., Heap, 2019) and a stepwise change in crustal porosity could be the origin of one, or perhaps both, of the intracrustal seismic discontinuities beneath the InSight landing site. One manner to reduce (or possibly remove) porosity, was proposed by Manga and Wright (2021). In their model, the precipitation of minerals in a liquid-water aquifer could have filled some of the pre-existing pore space. They estimated that under present-day conditions, liquid water could have once been stable at depths below 8–12 km near the InSight landing site. The shallowest intracrustal discontinuity at 8 km depth could thus represent a reduction in porosity associated with the top of an ancient aquifer.

As discussed in Section 6.2, pore space can also be removed at depth by viscous deformation of the host rock when the temperature is sufficiently elevated (e.g., Gyalay et al., 2020). Since viscosity is a strong function of temperature, the transition between unaffected porous materials and the complete closure of all pore space is predicted to occur over a very narrow depth interval of about a kilometer. If deep crustal porosity was the result of large impact basin forming events, as is believed to be the case on the Moon (Milbury et al., 2015; Wahl et al., 2020; Wicczorek et al., 2013), then the last major porosity forming events would be associated with

the youngest basins that formed near 3.9 Ga (Werner, 2008) in the Middle Noachian period, such as Isidis and Argyre. Using reasonable estimates of the heat flow and other parameters, the model of Gyalay et al. (2020) predicts that all porosity at depths greater than about 12–23 km would have been removed since this time. This range of depths is compatible with the second intracrustal seismic discontinuity at 20 km depth representing a transition from porous to non-porous materials.

6.3.3. Impact Ejecta

Large basin forming impact events would have generated thick ejecta deposits, and these could give rise to large scale layering within the crust of Mars. We make use of ejecta thickness estimates from the Orientale basin on the Moon as a guide for what might be expected beneath the InSight landing site. Based on the identification of impact craters that were partially buried by ejecta from Orientale, Fassett et al. (2011) showed that the ejecta thickness could be described by a power of distance normalized by the main crater rim radius. A thickness of almost 3 km was obtained near the rim, decreasing to about 400 and 130 m at respective distances of two and three normalized radii from the basin center.

The largest and closest impact basins to the InSight landing site are the Hellas, Isidis, and Utopia basins. Using the main rim diameters from Spudis (1993), we find that the InSight landing site is located at a distance of about four normalized radii from the centers of both the Hellas and Isidis basins, and only 1.1 radii from the center of the Utopia basin. Utopia basin should thus be by far the largest contributor of basin ejecta beneath the InSight lander. Utopia is about five times larger than the Orientale basin, and this implies that the thickness of its ejecta there could be about 11 km (using the equation in Fassett et al., 2011). There is considerable uncertainty in this estimate given that the true size of the Utopia basin is difficult to estimate given its highly degraded nature. Nevertheless, it is conceivable that highly fractured ejecta from Utopia could be the origin of either the uppermost or middle crustal layer observed beneath the InSight lander.

6.3.4. Change in Rock Crystallinity

A stepwise change in rock crystallinity, such as is observed in the oceanic crust on Earth, is an alternative explanation for either the 8 or 20 km seismic discontinuity on Mars. The oceanic crust possesses three layers with an average total thickness of about 6 km. The first interface corresponds to a transition from sedimentary to fine-grained extrusive basaltic rocks while the second interface is interpreted as a lithologic boundary between the fine-grained basaltic sheeted dikes that delivered melt to the surface and underlying coarse-grained gabbroic rocks that crystallized more slowly (Christeson et al., 2019). The thickness of the lowest layer of coarse-grained rocks is on average about 2–3 times larger than the overlying layer of fine-grained rocks. Though it is unlikely that the northern lowlands formed in the same manner as the oceanic crust on Earth, we note that the relative thicknesses of the crustal layers on Mars are inconsistent with the relative thicknesses of the oceanic crustal layers.

6.3.5. Magmatic Intrusive Rocks

Partial melting of the mantle gives rise to basaltic melts, some of which eventually erupt at the surface. Given the high iron content of typical Martian basalts, we compute that they would have had magma densities between about 2,700 and 2,900 kg m⁻³, which is comparable to our range of maximum permissible densities of the crust (2,850–3,100 kg m⁻³). The densest of these magmas would have had a tendency to accumulate near the base of the crust where they would be neutrally buoyant. Fractional crystallization of these magmas at depth would give rise to more evolved compositions that could either rise to form plutonic rocks at various levels in the crust or erupt at the surface (e.g., McCubbin et al., 2008; Udry et al., 2018, 2020).

The ultramafic cumulates resulting from the fractional crystallization of these magmas would be composed primarily of olivine and orthopyroxene, and their densities would be comparable to that of the underlying mantle. They could even potentially delaminate from the crust and recycle into the mantle provided the right geodynamic conditions. However, even if these cumulates were to remain at the base of the crust, given their ultramafic composition, they would be difficult to distinguish from upper mantle materials based solely on their density and seismic velocity. Thus, even if present at the base of the crust today, such ultramafic cumulates are unlikely to be the cause of any of the major seismic discontinuities observed beneath the InSight lander.

6.3.6. Differentiation of a Borealis Impact Melt Sheet

A popular model for the origin of the dichotomy boundary is that the northern lowlands represent the scar of a giant Borealis impact event that occurred early in Martian history (e.g., Andrews-Hanna et al., 2008; Marinova et al., 2008; Nimmo et al., 2008). This event would have excavated the entire pre-existing crust and would have generated a deep pool of impact melt. The thickness of this impact melt sheet would depend upon the impact velocity and impact angle, and could range from several tens to a couple hundred kilometers (Marinova et al., 2011). The resulting impact melt sheet would likely have partially differentiated to form a crust and complementary mafic cumulates, but the final thickness and composition of the crust, as well as any large-scale layering that might exist beneath the surface, are largely unstudied for basins of this size.

Koeppel et al. (2019) investigated the differentiation of impact melt sheets of smaller basins, showing that evolved compositions could be generated that are consistent with the felsic rocks found at Gale crater and in the meteorite NWA 7034. They showed that the general crystallization sequence for the thickest melt sheets is olivine → orthopyroxene → clinopyroxene → plagioclase. Depending on a variety of factors, including crystal segregation and the relative importance of fractional and equilibrium crystallization, such a crystallization sequence could perhaps result in a uniform composition crust, a crust that is zoned in composition, or a crust with distinct compositional layers. Lacking further modeling, it is difficult to assess whether this process is responsible for any of the layering observed beneath the InSight lander. Regardless, the composition of the resulting crust in the northern lowlands crust would almost certainly be different than that of the surrounding highlands.

6.3.7. Layering in the Southern Highlands From Borealis Ejecta

One major consequence of the Borealis impact is that it would have deposited a significant amount of ejecta in what is now the southern highlands of Mars. The ejecta would be composed of a mixture of crustal materials from all depths, upper mantle materials, and impact melts of both the crust and mantle. These materials would likely have been highly brecciated and might perhaps have been similar to the components that make up the NWA 7034 polymict breccia. This ejecta would have been deposited on top of the pre-existing crust of the southern highlands, and a simple mass balance estimate indicates that this deposit could be on average about 25 km thick (Citron & Zhong, 2012). Nevertheless, the spatial distribution of this ejecta is expected to be highly sensitive to the impact angle and impact velocity of this event (Marinova et al., 2008, 2011). Though we are currently lacking seismic constraints on the structure of the crust in the southern highlands, it is conceivable that a major seismic discontinuity there could be associated with the base of the Borealis ejecta deposit.

6.3.8. Crustal Magnetism

One last aspect that bears on the origin of layering within the crust comes from analyses of the magnetic field of Mars. The crustal magnetic field that is observed today is a remanent field carried by magnetic minerals in the crust, such as magnetite, pyrrhotite, and/or hematite (e.g., Dunlop & Arkani-Hamed, 2005). These materials were likely magnetized in the presence of a long-lived or intermittent core-dynamo field that operated between at least 4.5 and 3.7 Ga (Mittelholz et al., 2020), and their distribution informs us as to how these rocks formed. The magnetization depths were constrained by Gong and Wieczorek (2021) who made use of a localized magnetic field power spectrum analysis. In general, the average magnetization depth was found to be shallower in the northern lowlands than in the southern highlands, with respective depths of 9 and 32 km.

If the average magnetization depth of 9 km for the northern lowlands is interpreted as an equivalent thick magnetic layer that extends to the surface, the magnetic materials could extend to a depth of about 18 km. This depth coincides approximately with the 20 km seismic discontinuity, and suggests that the upper two crustal layers beneath the InSight lander could host the magnetized materials. Volcanic materials and ejecta from the Utopia basin in these two crustal layers could have acquired a thermoremanent magnetization when they were deposited. Hydrothermal alteration and serpentinization of crustal materials is another way to produce magnetite and magnetize the upper 20 km of the crust (e.g., Quesnel et al., 2009). The absence of detectable magnetization in the deepest layer beneath the InSight lander could reflect low quantities of magnetic minerals in this layer.

In contrast, if the average 32 km depth of magnetization of the southern highlands is interpreted in terms of an equivalent thick layer that extends to the base of the crust, this layer would extend upward to a depth of 20 km. Gong and Wieczorek (2021) hypothesized that the origin of this deep magnetization could be ancient magnetized crust that was subsequently buried by approximately 20 km of ejecta from the Borealis impact. In this

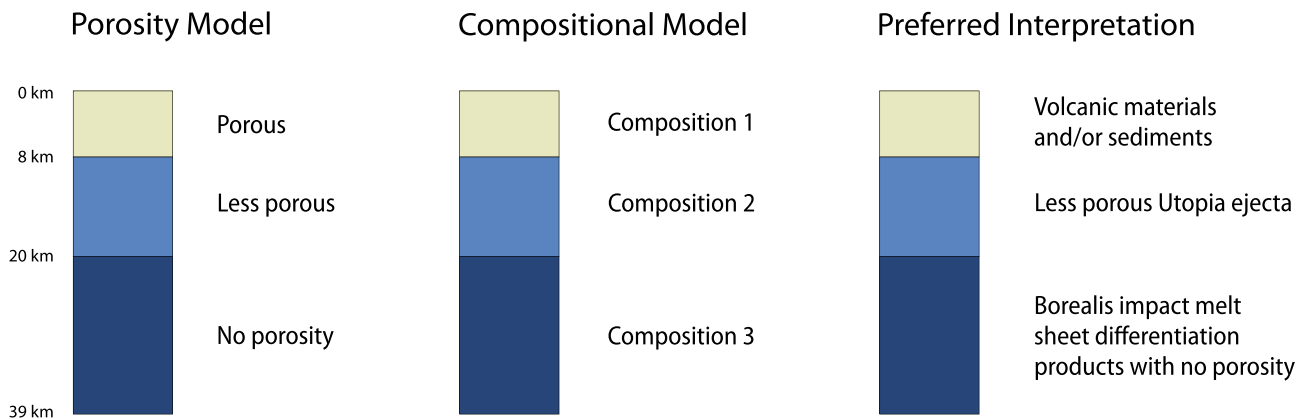


Figure 7. Interpretations of crustal layering beneath the InSight landing site. In the first two schematics, the crustal layering is a result either of stepwise changes in porosity (left) or composition (center). Our preferred interpretation combines elements of both of these end-member models. The depth of each seismic interface below the surface is denoted on the left schematic.

interpretation, variations in the depth of magnetization in the southern highlands would reflect variations in the thickness of Borealis ejecta.

6.3.9. A Possible Interpretation of Crustal Layering

One could interpret the crustal layering beneath the InSight landing site as being a result of either stepwise changes in porosity or stepwise changes in chemical composition. Here, we summarize one plausible interpretation of the large-scale stratigraphy of the crust both north and south of the dichotomy boundary that combines elements of both of these end-member models (see Figure 7). Future studies that investigate the scattering attenuation characteristics of the Martian crust and mantle (e.g., Karakostas et al., 2021; Menina et al., 2021) will be key for testing this proposed model.

In the northern lowlands, the upper 8 km of the crust could potentially be the result of thick sequences of volcanic materials that were deposited in the early Hesperian, Noachian, and pre-Noachian periods. To account for the low seismic velocities of this layer, either the extrusive lavas would need to be heavily fractured or the near-surface lava flows would need to cover thick pyroclastic deposits similar to the Medusae Fossae formation. Given the long duration over which these materials were emplaced, intercalated sedimentary deposits could be common and these materials might also have undergone substantial aqueous alteration at a later date (Lognonné et al., 2020). If there was a core dynamo operating when the volcanic rocks were deposited, they could have acquired a thermoremanent magnetization as they cooled. Ancient impact ejecta deposits from the Utopia basin are likely to be found below the layer of volcanic and sedimentary deposits, potentially in the middle layer between 8 and 20 km depth. At least part of the observed increase in seismic velocity at 8 km depth could be the result of a reduction in pore space from aqueous alteration products. The circulation of fluids in this initially porous aquifer could have led to the formation of magnetite that could have acquired a chemical remanent magnetization if there was a dynamo field present at the time. The increase in velocity at 20 km depth is likely to be a consequence of the complete viscous closure of all remaining pore space at about 4 Ga when the crustal temperatures were elevated. The deepest layer, from depths of 20–39 km, likely corresponds to the initial crust that formed during the differentiation of the Borealis impact melt sheet.

The expected stratigraphy of the southern highlands is less certain. Nevertheless, we speculate that a 20 km seismic discontinuity would be found there as well that represents the transitions from porous to non-porous materials. Another major discontinuity that is likely to be present in the southern highlands would be the base of thick ejecta deposits derived from the ancient Borealis impact event.

6.4. The Origin and Evolution of the Crust of Mars

The discovery of felsic rocks on Mars from in situ measurements and felsic clasts in the polymict breccia NWA 7034 (and its pairings) both indicate that ancient evolved crustal rocks are likely to be more prevalent than once thought. These evolved compositions could be the result of several processes, including low-degree partial

melting of the mantle, fractional crystallization of basaltic primary melts, differentiation of a thick impact melt sheet, or partial melting of a basaltic crust (e.g., Koepfel et al., 2019; McCubbin et al., 2008; Sautter et al., 2016; Udry et al., 2018, and references therein). Though the age distribution of these felsic materials is uncertain at this time, at least some of these rocks could be candidates for the primary crust of Mars that formed during its initial differentiation. For a general review of planetary crusts, their compositions, and the manner by which they formed, the reader is referred to Taylor and McLennan (2009) and McLennan (2022).

Zircons in the meteorite NWA 7034 have been found to be extremely ancient with ages between 4.39 and 4.47 Ga (Bellucci et al., 2015; Bouvier et al., 2018; Humayun et al., 2013; McCubbin et al., 2016). Lu-Hf isotopic analyses of these zircons imply that they likely crystallized from magmas with an andesite-like source that formed initially near 4.547 Ga (Bouvier et al., 2018) and U-Pb isotopic analyses indicate that they were derived from a geochemical reservoir that is significantly more enriched than the source of the younger Martian meteorites (Bellucci et al., 2015). Sm-Nd ages of the igneous lithologies that make up the matrix component of NWA 7034 yield a crystallization age of about 4.44 Ga (Nyquist et al., 2016) that is within the range of the zircon ages. The rare-earth element concentrations of the matrix components also imply a derivation from an enriched reservoir, with estimated concentrations of the parental melts being 100–1,000 times greater than CI chondrites (Nyquist et al., 2016). Given the ancient age of NWA 7034, it is likely derived from the ancient southern highlands of Mars. If it is representative of the materials found there, then this would indicate that the highlands represent an important geochemical reservoir of ancient enriched crustal materials.

Geochemical and isotopic compositions of Martian basaltic meteorites may be interpreted in a number of ways but are consistent with the existence of a significant reservoir of early enriched crustal rocks (e.g., Debaille et al., 2007; Norman, 1999). A variety of long-lived radiogenic isotope systems (e.g., Rb-Sr, Sm-Nd, Lu-Hf, Re-Os, U-Pb) and other geochemical parameters (e.g., fO_2 estimates) indicate derivation of basaltic shergottites by mixing of three or more distinct geochemical reservoirs (for a recent review, see Udry et al., 2020). At least two depleted reservoirs are widely interpreted as depleted mantle sources, however an enriched reservoir (i.e., high Rb/Sr, low Sm/Nd) could represent either enriched mantle, possibly related to trapped residual liquids during magma ocean crystallization (Armytage et al., 2018; Lapen et al., 2010), and/or an enriched crustal reservoir.

In one model that assumed the crust was the enriched end-member, Norman (1999) calculated the rare-earth element and Nd-isotope mass balance between depleted mantle and enriched crust for the shergottites. The inferred isotopic compositions of the two end-members constrained the relative abundances of Nd in the two reservoirs, and the thickness of the crust controlled the absolute abundances of Nd in the two reservoirs. The derived crustal composition based on the enriched meteorite Shergotty implied a global equivalent thickness of the enriched crustal component to be less than 45 km, with a best-fitting range of 20–30 km. For the same mixing model, the crustal Nd concentration (9.4 ppm) estimated by Taylor and McLennan (2009) leads to a crustal thickness of 50 km. When combined with our independent constraints on the average thickness of the crust, these results are thus consistent with at least one-third of the present-day crust being composed of these ancient enriched materials, with the remainder being younger magmatic materials that were likely derived from the depleted mantle. If some portion of the enriched geochemical reservoir is located in the mantle, the above mass-balance calculations would require a thinner enriched crust.

Additional support for the existence of an enriched crustal reservoir comes from both in situ and orbital analyses of Martian surface materials. Mars Odyssey gamma ray spectroscopy data show that the average surface composition is more enriched in incompatible and heat producing elements than nearly all of the known Martian meteorites (Taylor et al., 2006). Whereas K abundances of the meteorites range between about 200 and 2,600 ppm, surface compositions as viewed from orbit range from about 2,000 to 6,000 ppm. If the gamma ray derived surface compositions are representative of the underlying crust, our range of crustal thicknesses imply that between 30% and 70% of all heat producing elements should be in the crust (see also McLennan, 2003; McLennan, 2022). In situ compositions of soils from rovers (McLennan, 2001; Taylor & McLennan, 2009) indicate similarly that about 50% of the incompatible elements reside in the Martian crust. Thermal evolution simulations that can account for recent volcanism on Mars and present-day estimates of the thickness of the elastic lithosphere also indicate a similar heat-producing element distribution with more than 50% of its bulk content in the crust (Plesa et al., 2018; Thiriet et al., 2018). Lastly, thermal evolution simulations that account for lateral variations in crustal thickness, InSight seismic constraints, and only localized melting at the present day require that the crust contain 55%–70% of the bulk heat producing elements (Knappmeyer-Endrun et al., 2021).

Several lines of evidence suggest that crust formation on Mars occurred very early in its evolution. Initial metal-silicate differentiation would have formed a metal core when Mars was accreting. Based on Hf-W isotopic data (Dauphas & Pourmand, 2011), about 90% of the planet is predicted to have accreted in the first 1.5–6 My after the formation of the first solids in the solar system (i.e., the calcium aluminum-rich inclusions that are dated to 4.567 Ga, Connelly et al., 2012). At this early time, the protoplanet would have been largely molten given the heat released from the short-lived radionuclide ^{26}Al , and this would have facilitated metal-silicate fractionation (see discussion in Elkins-Tanton et al., 2005). Silicate differentiation into depleted and enriched reservoirs is believed to have occurred shortly after core formation. An analysis of both W and Nd isotopic compositions of Martian materials shows that this occurred over the prolonged period from about 20 to 40 My after solar system formation, between about 4.53 and 4.55 Ga (Kruijer et al., 2017). This range of ages is compatible with the inferred age of the enriched andesitic-source materials from which the zircons in NWA 7034 were derived (Bouvier et al., 2018). In order to account for the crystallization ages of these zircons, as well as the crystallization age of the matrix materials in this rock, these source materials would then need to have been remelted and reprocessed several times, plausibly during impact events, over an almost 100 My time span between 4.39 and 4.47 Ga (Armytage et al., 2018; Bellucci et al., 2015; Bouvier et al., 2018; Humayun et al., 2013; McCubbin et al., 2016).

The processes responsible for creating an early crust on Mars are not well understood, but they are likely related to the final stages of magma ocean crystallization. Fractional crystallization of such a magma ocean would have had two major consequences. First, the final liquids to crystallize would have been highly enriched in incompatible and heat producing elements and would represent the enriched complement to the depleted mantle cumulates. Second, the mantle cumulates would have been initially gravitationally unstable, with dense iron-rich materials overlying less dense magnesian materials (Elkins-Tanton et al., 2003). These cumulates would have overturned, and in the process, some of the rising cumulates would have partially melted, perhaps contributing to the formation of an early crust (Elkins-Tanton et al., 2005). It is important to emphasize, however, that the crustal materials formed during such an overturn event would have been derived from the depleted mantle, and would not represent the enriched reservoir of crustal materials that is required to account for the Nd and U-Pb isotopic data.

In the model of Elkins-Tanton et al. (2005), it was argued that the vast majority of the late stage cumulates would probably have sunk to the base of the mantle, forming an enriched geochemical reservoir that has since remained isolated from the rest of the mantle. Nevertheless, they acknowledged that at least a portion of the late stage magma ocean materials could have survived near the surface, especially if their highly evolved felsic and hydrous compositions were buoyant with respect to the underlying cumulates when they formed. The existence of rocks like NWA 7034 suggest that at least some portion of these early enriched compositions did in fact survive to form part of an early primary crust. Nevertheless, the relationship between this enriched crust and the enriched reservoir that could have been incorporated into the mantle remains unclear (e.g., Armytage et al., 2018).

Following core and primary crust formation, the next major event in Martian history would have been the impact event that formed that Borealis basin. This event is responsible for creating the large scale morphology of the planet that is still visible today, including the northern lowlands that represents a 10,000 km diameter impact scar. This impact would have completely excavated the preexisting crust there, and would have deposited a significant amount of ejecta in the surroundings, forming what is now the thickened crust of the southern highlands. This ejecta would be composed not only of the initial primary crustal materials at the impact site, but also ultramafic materials from the upper mantle. Initially, a thick impact melt pool would have been present in the basin interior, and the crystallization of this melt pool would almost certainly have formed new crustal materials. In all likelihood, the abundances of heat producing elements in this newly formed crust would be significantly less than that of the primary crust of Mars given that it would have been generated from a depleted mantle composition. Though the age of the Borealis impact is not known, the 4.44 Ga crystallization age of the matrix components in NWA 7034, or any of the 4.39–4.47 Ga zircon ages, could plausibly date this event. A similar age has been proposed by Bottke and Andrews-Hanna (2017) that is based on highly siderophile element concentrations in the mantle that are plausibly derived from the Borealis impactor.

Subsequent to these major events, crust formation would have continued over geologic time by partial melting of the mantle. In contrast to the primary enriched crust of Mars, these magmatic products would have been largely derived from a depleted mantle source, with much of their compositional trends being explained by various degrees of fractional crystallization within the crust and variations in the source depth and temperature (e.g., Filiberto, 2017; Udry et al., 2020). Remote sensing data indicate that the oldest eruptive basalts in the Noachian

period generally have relatively high abundances of low-calcium pyroxene in comparison to high-calcium pyroxene, whereas for the younger basalts in the Hesperian and Amazonian high-calcium pyroxenes are the most abundant (e.g., Baratoux et al., 2013; Mustard et al., 2005; Poulet et al., 2009). This transition in pyroxene composition has been explained by a deepening of the thermal lithosphere of Mars with time (which gives rise to higher pressures of melting), and to the slow secular cooling of the Martian mantle (Baratoux et al., 2011).

The NWA 7034 meteorite, isotopic considerations, and the observed surface composition of Mars are all consistent with the existence of a major geochemical reservoir of enriched crustal materials. These materials naturally represent the enriched complement to the depleted mantle reservoir that later gave rise to the magmatic materials sampled by the Martian basaltic meteorites. Based on the compositions of the lithologies found in NWA 7034, as well as the evolved rocks of Gale crater, these ancient crustal materials are likely to be more felsic than the younger basaltic materials that cover much of the surface of Mars. The crust of Mars should thus not be viewed simply as a thick sequence of lava flows derived from partial melting of the mantle, but rather as an ancient primary crust that was buried in part by later basaltic magmas derived from a depleted mantle. The relative fraction of the enriched crustal materials and the later basaltic magmas is difficult to constrain, but the enriched component probably makes up more than a third of the total crust.

7. Conclusions

Prior to NASA's InSight mission, estimates for the thickness of the Martian crust came from a variety of indirect methods. These included the use of gravity and topography data, viscous relaxation simulations of surface topography, incompatible element mass-balance arguments, thermal evolution simulations that considered the partitioning of heat-producing elements between the crust and mantle, and combined modeling of the mass, moment of inertia, and tidal Love number. As summarized in Table 1, average thickness estimates varied from about 27 to 115 km. The InSight seismic investigation provided us with the first in situ estimate for the thickness of the crust of Mars (Knapmeyer-Endrun et al., 2021) in the northern lowlands of Mars, and this is an indispensable constraint for studies of the global character of the crust of Mars.

In this work, gravity and topography data were used to construct global crustal thickness models that satisfy the favored 3-layered crustal model beneath the InSight landing site, where the crustal thickness is 39 ± 8 km. Considering a broad range of possible mantle and core density profiles, as well as a range of average densities for the crust (including a potential change in density across the dichotomy boundary), our work firmly supports an average crustal thickness between 30 and 72 km. Furthermore, these models imply that the maximum permissible average density of the southern highlands and northern lowlands crust is, depending on the density of the upper mantle, somewhere between 2,850 and 3,100 kg m⁻³. The crustal thickness range we obtained is consistent with the upper limits provided by incompatible element mass-balance and viscous relaxation arguments (<118 km, Nimmo & Stevenson, 2001; Taylor et al., 2006; Zuber et al., 2000), and is very similar to the range obtained from modeling geoid-topography ratios under the assumption of Airy isostasy (31–81 km, Wieczorek & Zuber, 2004). Thermal evolution modeling, as well as studies that considered the moment of inertia, tidal Love number and thermodynamic modeling, are generally consistent with the range we obtain as well, but tend to prefer somewhat larger values (49–87 km, Plesa et al., 2018; Khan et al., 2018).

The broad range of average crustal thicknesses that we obtain is a result of several factors. First, the InSight crustal thickness constraint that we use has an uncertainty of 8 km. In all likelihood, this value will become more precise as the number of Martian quakes increases with time and as analysis techniques develop. Another source of uncertainty is the density of the upper mantle. New seismic events and further analyses of the InSight data will eventually be able to exclude some of the interior composition models that were considered in this study. If the uncertainty in the seismic thickness could be eliminated, and if only a single mantle density profile were considered, our range of average thicknesses would be reduced by a factor of about two.

The two parameters that have the largest impact on our global crustal thickness modeling are the bulk density and average thickness of the crust. With two unknowns and only one seismic constraint, it should not come as a surprise that these two model parameters can not be pinned down more precisely. Our models that consider a change in density across the dichotomy boundary are even less well constrained, with three effective unknowns. Fortunately, we do have a partial constraint at our disposal, which is that the crustal thickness can not be negative,

and it is this constraint that allowed us to obtain an upper bound on the crustal density. Nevertheless, if further progress is to be made, we will need additional seismic constraints at different places on the planet.

There are a few techniques that could provide additional seismic constraints on the thickness of the crust using InSight data. First, by modeling the PP wave, it may be possible to constrain the crustal thickness at the bounce point, which is located halfway between the seismic source and station. This would be constrained by the use of a precursor phase associated with the underside reflection from the crust-mantle interface at that point (e.g., Rychert & Shearer, 2010). Similar analyses could in principle be performed using other surface multiples from both the P and S waves. Second, identification and modeling of crustal phases from source-side structure would also improve the current marsquake moment tensors (e.g., Brinkman et al., 2021) and allow us to simultaneously invert for the underlying crustal structure. Third, if a sufficiently energetic impact event is detected, this would allow for the possibility of constraining the thickness of the crust at the impact site, in a similar manner as was done for the Moon (Chenet et al., 2006). Lastly, if surface waves are detected at relatively short periods (>20 s), this would allow us to determine more details about the average crustal structure using dispersion measurements (e.g., Khan et al., 2016; Panning et al., 2015).

Beyond using InSight seismic data, further constraints on the thickness of the Martian crust will likely have to wait for a future mission to place a second seismometer on the surface of the planet. Ideally, such a seismic station would be located in the southern highlands, where the crustal thickness is predicted to be significantly different than beneath the InSight lander. A crustal thickness determination beneath such a station would remove most of the ambiguity regarding the tradeoff between average crustal thickness and bulk crustal density. If the densities of the northern lowlands and southern highlands crust are different, then a third seismic station would be necessary to constrain more precisely the densities of these two terrains. An additional seismic station located within the Tharsis volcanic province would also prove useful, as this region is likely to be different in character from both the northern lowlands and southern highlands.

Appendix A: Crustal Thickness Inversion Procedure

The gravitational potential, U , exterior to the mass distribution of a planet can be expressed as a sum of spherical harmonic functions

$$U(\mathbf{r}) = \frac{GM}{r} \sum_{l=0}^{\infty} \sum_{m=-l}^l \left(\frac{R_0}{r}\right)^l C_{lm} Y_{lm}(\theta, \phi). \quad (\text{A1})$$

Here, Y_{lm} is a spherical harmonic function of degree l and order m , C_{lm} represents the corresponding spherical harmonic coefficients of the gravitational potential for a reference radius R_0 , G is the gravitational constant, and M is the total planetary mass. The function is evaluated at a radius r , co-latitude θ and longitude ϕ , and in practice the sum is truncated at a maximum spherical harmonic degree L that is determined by the data resolution. The spherical harmonic functions used here are normalized according to the geodesy convention (for a review, see Wicczorek, 2015).

We aim to construct of model of Mars that can satisfy the observed gravity field. For this, we assume that the observed spherical harmonic coefficients, C_{lm} , can be modeled as the result of several contributions

$$C_{lm} = C_{lm}^{\text{hydro}} + C_{lm}^{\text{topo}} + C_{lm}^{\text{ice}} + C_{lm}^{\phi} + C_{lm}^{\rho} + C_{lm}^{\text{cm}}, \quad (\text{A2})$$

each of which will be described separately in the subsections below. In practice, we attempt to satisfy all spherical harmonic degrees and orders, with the exception of the degree zero term, C_{00} . This term does not generate any lateral variations in the gravitational field and only contributes to the total mass of the planet. Fitting the total mass would require detailed modeling of the density and temperature profile of the mantle and core and would depend on a combination of independent data such as the moment of inertia, tides, nutations, and seismic arrival times (e.g., Folkner et al., 2018; Kahan et al., 2021). We truncate the gravity field of Mars at degree 90, given that the model we employ was regularized beyond this degree (Genova et al., 2016). Nevertheless, in order to avoid aliasing when computing the gravitational signals related to relief along density interfaces, all calculations were performed on grids that could resolve spherical harmonic degrees that were four times this value. When computing the predicted gravity using the finite-amplitude technique of Wicczorek and Phillips (1998), we consider

powers n of the relief up to 7. We note that the spherical harmonic coefficients of all terms in Equation A2 need to use the same reference radius as the observed gravity field.

A1. C_{lm}^{hydro}

The first contribution in Equation A2 is the gravitational signal from flattened hydrostatic interfaces beneath the rigid lithosphere. The procedure to compute this term is described in Wieczorek et al. (2019) and requires a 1-dimensional density model of the sub-lithospheric mantle and core. Furthermore, to account for the gravitational contributions coming from the non-hydrostatic rigid lithosphere, we need to assume the thickness of the elastic lithosphere, to make use of the known shape of the planet, to assume a density of the surface materials, and to assume an effective depth from where the remaining lithospheric gravitational anomalies arise. The largest component of the hydrostatic gravity signal is C_{20}^{hydro} , which depending on the density profile is about 4%–6% of the observed value (For comparison, the crustal thickness model of Neumann et al. (2004) only considered the signal coming from the core-mantle boundary, which is about 2% of the observed value.). Beyond the degree-2 term, the shapes of the hydrostatic density interfaces resemble that of the geoid, with relief up to 2 km in the upper mantle and attenuating to less than a kilometer at the core-mantle interface.

When computing the hydrostatic contribution from the mantle and core, we set the density of the surface materials to the average density of the crustal model. The depth of the gravity anomalies in the deeper lithosphere was assumed to be 44 km, which is comparable to the average crustal thickness of our models. Reasonable variations of these two parameters were found to affect the subsequent crustal thickness models by only about a kilometer (see also Wieczorek et al., 2019). The gravitational contribution from the sub-lithospheric mantle and core was computed up to a maximum spherical harmonic degree of 15, which is more than sufficient to capture the long-wavelength shape of hydrostatic interfaces.

A2. C_{lm}^{topo}

The second contribution in Equation A2 corresponds to the gravitational signal of surface relief on Mars, after having removed the polar caps (see the following section). The surface relief is referenced to the mean radius of the crust (excluding polar caps), and when the density of the crust is constant, this is computed using the finite-amplitude technique of Wieczorek and Phillips (1998). When considering lateral variations in crustal density, $\rho_c(\theta, \phi)$, we make use of the more general finite-amplitude calculation procedure as given by Wieczorek (2015):

$$C_{lm}^{topo} = \frac{4\pi D^3}{M(2l+1)} \sum_{n=1}^{l+3} \frac{(\rho_c h^n)_{lm}}{D^n n!} \frac{\prod_{j=1}^n (l+4-j)}{(l+3)}, \quad (\text{A3})$$

where h is the relief with respect to the average radius D of this interface. The coefficients in Equation A3 are referenced to the radius D , and hence need to be upward continued to the same reference radius used by the observed gravity model.

A3. C_{lm}^{ice}

The third contribution in Equation A2 is the gravitational signal that comes from the two polar ice caps. The polar caps are small, and thus were found to have a negligible impact on both the computed thickness of the crust at the InSight landing site and the average crustal thickness of our models. Nevertheless, given that the density of ice-rich materials is considerably less than typical crustal materials, if their lower than average densities were neglected, our models would predict an anomalously thick crust beneath the polar deposits.

We make use of the polar cap thickness models developed by Broquet et al. (2020); Broquet et al. (2021) that considered lithospheric flexure and orbital radar constraints. For the north polar cap, we used a representative model with a bulk density of $1,250 \text{ kg m}^{-3}$ and an elastic thickness of 330 km. For the south polar cap, we used a model with a bulk density of $1,300 \text{ kg m}^{-3}$ and an elastic thickness of 175 km. To compute the gravitational attraction of the two polar caps we first computed the gravitational signal using the observed shape of the planet with a density ρ_{ice} . Then, the gravity signal resulting from the shape of the surface, excluding the polar cap, was subtracted using the same density.

A4. C_{lm}^ϕ

The fourth contribution in Equation A2 corresponds to the gravitational signal of a layer of constant thickness with density ρ_ϕ that extends from the surface (excluding the polar caps) to a depth d . In practice, the density of this layer is parameterized in terms of porosity ϕ , where $\rho_\phi = (1 - \phi)\rho_c$. Given that we have already accounted for the gravitational signal of the surface relief C_{lm}^{topo} using a density ρ_c , we need only to add a negative signal coming from this layer using an effective density contrast of $\rho_\phi - \rho_c$.

The gravitational signal of this layer was computed in an analogous manner to that of the polar caps. First the gravity resulting from the surface relief was computed using the specified density contrast, and then the gravity signal from the relief at depth d was subtracted using the same density contrast. Whenever this low density layer extended into the mantle, the contribution from the anomalous mantle density, $\phi\rho_m$, was calculated separately. Given that the thickness of the layer is constant, the gravity signal from the top and bottom of the layer are very similar and the resulting term is very small.

A5. C_{lm}^ρ

The fifth contribution in Equation A2 corresponds to the gravitational signal resulting from lateral variations in density of the crust. As we have already accounted for lateral variations in density of the surface relief (with respect to the mean planetary radius R), and that we will also account for lateral variations in relief along the crust-mantle interface at an average depth R_{cm} , we only need to account for the signal arising in a spherical shell bounded by R and R_{cm} . It is straightforward to compute this contribution analytically, and the spherical harmonic coefficients are given by (see also Wicczorek et al., 2013)

$$C_{lm}^\rho = \frac{4\pi R^3}{M(2l+1)(l+3)} (1 - (R_{cm}/R)^{l+3}) \rho_{lm}, \quad (\text{A4})$$

where ρ_{lm} are the spherical harmonic coefficients of $\rho(\theta, \phi)$. These potential coefficients are referenced to the radius R and need to be upward continued to the reference radius of the gravity model.

A6. C_{lm}^{cm}

The last contribution to Equation A2 corresponds to the gravitational signal resulting from relief along the crust-mantle interface. The gravity of this relief is calculated in the same manner as for the surface. In particular, we simply make use of the equation for the finite-amplitude correction of Equation A3, replacing h with the shape of the crust-mantle interface and ρ with $\rho_m - \rho_c(\theta, \phi)$, where ρ_m is the density of the uppermost mantle. In contrast to the other terms of Equation A2 that are known a priori, as described in the following section, we need to determine numerically the relief along the crust-mantle interface that satisfies the observed gravity field.

A7. Crust-Mantle Relief Determination

All of the terms in Equation A2 can be computed using priori knowledge with the exception of the term involving the relief along the crust-mantle interface. We define the Bouguer anomaly as the gravitational signal that remains after removing all quantifiable contributions from the observed free-air gravity:

$$C_{lm}^{BA} = C_{lm} - C_{lm}^{hydro} - C_{lm}^{topo} - C_{lm}^{ice} - C_{lm}^\phi - C_{lm}^\rho. \quad (\text{A5})$$

Following the approach of Wicczorek and Phillips (1998) and Wicczorek et al. (2013), we set C_{lm}^{cm} equal to C_{lm}^{BA} and then separate the first-order term of the crust-mantle relief from the terms that involve higher powers of the relief. Given that the resulting equation effectively requires that the Bouguer anomaly be evaluated at the crust-mantle interface, a downward continuation filter w_l is introduced that attenuates the short-wavelength signals that are exponentially amplified with depth. The resulting equation can be written as

$$\left({}^{(i+1)}h \Delta\rho \right)_{lm} = w_l \left[\frac{C_{lm}^{BA} M (2l+1)}{4\pi R_{cm}^2} \left(\frac{R}{R_{cm}} \right)^l - R_{cm} \sum_{n=2}^N \frac{{}^{(i)}h^n \Delta\rho_{lm}}{R_{cm}^n n!} \frac{\prod_{j=1}^n (l+4-j)}{(l+3)} \right], \quad (\text{A6})$$

where $\Delta\rho$ is defined as $\rho_m - \rho_c(\theta, \phi)$. This equation is solved in an iterative manner, where the term $i = 0$ on the right side is initially set to zero, which provides an initial first-order estimate of $(h\Delta\rho)_{im}$ on the left hand side. The relief h is obtained by expanding this function on a grid and dividing by the known function $\Delta\rho$. To stabilize oscillations between successive iterations, and to speed convergence, the following iterative scheme is used:

$${}^{(i+3)}h = ({}^{(i+2)}h + {}^{(i+1)}h) / 2, \quad (\text{A7})$$

$${}^{(i+4)}h = f({}^{(i+3)}h), \quad (\text{A8})$$

where f represents schematically the above-described calculation of ${}^{(i+1)}h$. For the filter w_p , we make use of the minimum amplitude filter of Wieczorek and Phillips (1998). Without such a filter, either noise in the gravity field or imperfect modeling of the contributions in Equation A5 would give rise to unrealistic oscillations of the function h . This filter is designed to have an amplitude of 0.5 at degree 50, which is a choice used by previous investigations (e.g., Baratoux et al., 2014; Smrekar et al., 2019; Wieczorek et al., 2019).

Data Availability Statement

All results presented in the figures and tables of this work can be reproduced using the example scripts *Mars-Crust-InSight.py* and *Mars-Crust-InSight-dichotomy.py* in the python-based open-source software *ctplanet* (Wieczorek, 2021). The spherical harmonic coefficients of the crust-mantle interface for all models, gridded datasets for the models presented in Figures 2 and 6, and a spreadsheet that summarizes all the models are available at Wieczorek (2022). The spherical harmonic coefficients can be manipulated and converted to grids using the open-source software *pyshtools* (Wieczorek & Meschede, 2018).

Acknowledgments

The French authors acknowledge the French Space Agency (CNES) and the French National Research Agency (ANR-14-CE36-0012-02 and ANR-19-CE31-0008-08) for funding the InSight science analysis. A portion of the work was done by the InSight Project, Jet Propulsion Laboratory, California Institute of Technology, under a contract with the National Aeronautics and Space Administration. CM and DA have received funding from the European Research Council (ERC) under the European Union's Horizon 2020 research and innovation programme (grant agreements 101001689 and 724690, respectively). We thank J. Andrews-Hanna for providing us with a digital mask of the Tharsis plateau. We also thank G. Jeff Taylor and an anonymous reviewer for comments that helped improve this manuscript. Discussions with Julia Maia and Benjamin Bultel helped improve various aspects of this manuscript. This is InSight contribution 243.

References

- Anderson, D. L., Miller, W. F., Latham, G. V., Nakamura, Y., Toksöz, M. N., Dainty, A. M., et al. (1977). Seismology on Mars. *Journal of Geophysical Research*, 82(28), 4524–4546. <https://doi.org/10.1029/JS082i028p04524>
- Andrews-Hanna, J. C., Zuber, M. T., & Banerdt, W. B. (2008). The Borealis basin and the origin of the Martian crustal dichotomy. *Nature*, 453(7199), 1212–1215. <https://doi.org/10.1038/nature07011>
- Armytage, R. M. G., Debaille, V., Brandon, A. D., & Agee, C. B. (2018). A complex history of silicate differentiation of Mars from Nd and Hf isotopes in crustal breccia NWA 7034. *Earth and Planetary Science Letters*, 502, 274–283. <https://doi.org/10.1016/j.epsl.2018.08.013>
- Babeyko, A., & Zharkov, V. N. (2000). Martian crust: A modeling approach. *Physics of the Earth and Planetary Interiors*, 117(1–4), 421–435. [https://doi.org/10.1016/S0031-9201\(99\)00111-9](https://doi.org/10.1016/S0031-9201(99)00111-9)
- Banerdt, W. B., Smrekar, S. E., Banfield, D., Giardini, D., Golombek, M., Spiga, A., et al. (2020). Initial results from the InSight mission on Mars. *Nature Geoscience*, 13(3), 183–189. <https://doi.org/10.1038/s41561-020-0544-y>
- Baratoux, D., Samuel, H., Michaut, C., Toplis, M. J., Monnerneau, M., Wieczorek, M., et al. (2014). Petrological constraints on the density of the Martian crust. *Journal of Geophysical Research: Planets*, 119(7), 1707–1727. <https://doi.org/10.1002/2014JE004642>
- Baratoux, D., Toplis, M. J., Monnerneau, M., & Gasnault, O. (2011). Thermal history of Mars inferred from orbital geochemistry of volcanic provinces. *Nature*, 472(7343), 338–341. <https://doi.org/10.1038/nature09903>
- Baratoux, D., Toplis, M. J., Monnerneau, M., & Sautter, V. (2013). The petrological expression of early Mars volcanism. *Journal of Geophysical Research: Planets*, 118(1), 59–64. <https://doi.org/10.1029/2012JE004234>
- Belleguic, V., Lognonné, P., & Wieczorek, M. (2005). Constraints on the Martian lithosphere from gravity and topography data. *Journal of Geophysical Research*, 110(E11), E11005. <https://doi.org/10.1029/2005JE002437>
- Bellucci, J., Nemchin, A., Whitehouse, M., Humayun, M., Hewins, R., & Zanda, B. (2015). Pb-isotopic evidence for an early, enriched crust on Mars. *Earth and Planetary Science Letters*, 410, 34–41. <https://doi.org/10.1016/j.epsl.2014.11.018>
- Besserer, J., Nimmo, F., Wieczorek, M. A., Weber, R. C., Kiefer, W. S., McGovern, P. J., et al. (2014). GRAIL gravity constraints on the vertical and lateral density structure of the lunar crust. *Geophysical Research Letters*, 41(16), 5771–5777. <https://doi.org/10.1002/2014GL060240>
- Beuthe, M., Maistre, S. L., Rosenblatt, P., Pätzold, M., & Dehant, V. (2012). Density and lithospheric thickness of the Tharsis Province from MEX Mars and MRO gravity data. *Journal of Geophysical Research*, 117(E4), E04002. <https://doi.org/10.1029/2011JE003976>
- Borg, L., & Drake, M. J. (2005). A review of meteorite evidence for the timing of magmatism and of surface or near-surface liquid water on Mars. *Journal of Geophysical Research*, 110(E12), E12S03. <https://doi.org/10.1029/2005JE002402>
- Botke, W. F., & Andrews-Hanna, J. C. (2017). A post-accretionary lull in large impacts on early Mars. *Nature Geoscience*, 10(5), 344–348. <https://doi.org/10.1038/NGEO2937>
- Bouvier, L. C., Costa, M. M., Connelly, J. N., Jensen, N. K., Wielandt, D., Storey, M., et al. (2018). Evidence for extremely rapid magma ocean crystallization and crust formation on Mars. *Nature*, 558(7711), 586–589. <https://doi.org/10.1038/s41586-018-0222-z>
- Boynton, W. V., Taylor, G. J., Evans, L. G., Reedy, R. C., Starr, R., Janes, D. M., et al. (2007). Concentration of H, Si, Cl, K, Fe, and Th in the low- and mid-latitude regions of Mars. *Journal of Geophysical Research*, 112(E12), E12S99. <https://doi.org/10.1029/2007JE002887>
- Brinkman, N., Stähler, S. C., Giardini, D., Schmelzbach, C., Khan, A., Jacob, A., et al. (2021). First focal mechanisms of Marsquakes. *Journal of Geophysical Research: Planets*, 126(4), e2020JE006546. <https://doi.org/10.1029/2020JE006546>
- Broquet, A., & Wieczorek, M. A. (2019). The gravitational signature of Martian volcanoes. *Journal of Geophysical Research: Planets*, 124(8), 2054–2086. <https://doi.org/10.1029/2019JE005959>
- Broquet, A., Wieczorek, M. A., & Fa, W. (2020). Flexure of the lithosphere beneath the north polar cap of Mars: Implications for ice composition and heat flow. *Geophysical Research Letters*, 47(5), e2019GL086746. <https://doi.org/10.1029/2019GL086746>

- Broquet, A., Wieczorek, M. A., & Fa, W. (2021). The composition of the south polar cap of Mars derived from orbital data. *Journal of Geophysical Research: Planets*, 126(8), e2020JE006730. <https://doi.org/10.1029/2020JE006730>
- Brückner, J., Dreibus, G., Rieder, R., & Wänke, H. (2003). Refined data of alpha proton x-ray spectrometer analyses of soils and rocks at the Mars Pathfinder site: Implications for surface chemistry. *Journal of Geophysical Research*, 108(E12), 8094. <https://doi.org/10.1029/2003JE002060>
- Carter, J., & Poulet, F. (2013). Ancient plutonic processes on Mars inferred from the detection of possible anorthositic terrains. *Nature Geoscience*, 6(12), 1008–1012. <https://doi.org/10.1038/NGEO1995>
- Chenet, H., Lognonné, P., Wieczorek, M., & Mizutani, H. (2006). Lateral variations of lunar crustal thickness from the Apollo seismic data set. *Earth and Planetary Science Letters*, 243(1–2), 1–14. <https://doi.org/10.1016/j.epsl.2005.12.017>
- Cheung, K. K., & King, S. D. (2014). Geophysical evidence supports migration of Tharsis volcanism on Mars. *Journal of Geophysical Research: Planets*, 119(5), 1078–1085. <https://doi.org/10.1002/2014JE004632>
- Christensen, P. R., McSween, H. Y., Jr., Bandfield, J. L., Ruff, S. W., Rogers, A. D., Hamilton, V. E., et al. (2005). Evidence for magmatic evolution and diversity on Mars from infrared observations. *Nature*, 436(7050), 504–509. <https://doi.org/10.1038/nature03639>
- Christeson, G. L., Goff, J. A., & Reece, R. S. (2019). Synthesis of oceanic crustal structure from two-dimensional seismic profiles. *Reviews of Geophysics*, 57(2), 504–529. <https://doi.org/10.1029/2019RG000641>
- Citron, R. L., & Zhong, S. (2012). Constraints on the formation of the Martian crustal dichotomy from remnant crustal magnetism. *Physics of the Earth and Planetary Interiors*, 212–213, 55–63. <https://doi.org/10.1016/j.pepi.2012.09.008>
- Connell, J. N., Bizzarro, M., Krot, A. N., Nordlund, A., Wielandt, D., & Ivanova, M. A. (2012). The absolute chronology and thermal processing of solids in the solar protoplanetary disk. *Science*, 338(6107), 651–655. <https://doi.org/10.1126/science.1226919>
- Consolmagno, G., Britt, D., & Macke, R. (2008). The significance of meteorite density and porosity. *Chemie der Erde—Geochemistry*, 68, 1–29. <https://doi.org/10.1016/j.chemer.2008.01.003>
- Cousin, A., Sautter, V., Payré, V., Forni, O., Mangold, N., Gasnault, O., et al. (2017). Classification of igneous rocks analyzed by ChemCam at Gale crater, Mars. *Icarus*, 288, 265–283. <https://doi.org/10.1016/j.icarus.2017.01.014>
- Dauphas, N., & Pourmand, A. (2011). Hf–W–Th evidence for rapid growth of Mars and its status as a planetary embryo. *Nature*, 473(7348), 489–492. <https://doi.org/10.1038/nature10077>
- Debaillie, V., Brandon, A. D., Yin, Q. Z., & Jacobsen, B. (2007). Coupled 142Nd–143Nd evidence for a protracted magma ocean in Mars. *Nature*, 450(7169), 525–528. <https://doi.org/10.1038/nature06317>
- Ding, M., Lin, J., Gu, C., Huang, Q., & Zuber, M. T. (2019). Variations in Martian lithospheric strength based on gravity/topography analysis. *Journal of Geophysical Research: Planets*, 124(11), 3095–3118. <https://doi.org/10.1029/2019JE005937>
- Dunlop, D. J., & Arkani-Hamed, J. (2005). Magnetic minerals in the Martian crust. *Journal of Geophysical Research*, 110(E9), E12S04. <https://doi.org/10.1029/2005JE002404>
- Durán, C., Khan, A., Ceylan, S., Zenhäuser, G., Stähler, S., Clinton, J. F., & Giardini, D. (2022). Seismology on Mars: An analysis of direct, reflected, and converted seismic body waves with implications for interior structure. *Physics of the Earth and Planetary Interiors*, 325, 106851. <https://doi.org/10.1016/j.pepi.2022.106851>
- Edwards, P. H., Bridges, J. C., Wiens, R., Anderson, R., Dyar, D., Fisk, M., et al. (2017). Basalt–trachybasalt samples in Gale crater, Mars. *Meteoritics & Planetary Sciences*, 52, 2391–2410. <https://doi.org/10.1111/maps.12953>
- Ehlmann, B. L., & Edwards, C. S. (2014). Mineralogy of the martian surface. *Annual Review of Earth and Planetary Sciences*, 42(1), 291–315. <https://doi.org/10.1146/annurev-earth-060313-055024>
- Ehlmann, B. L., Mustard, J. F., Swayze, G. A., Clark, R. N., Bishop, J. L., Poulet, F., et al. (2009). Identification of hydrated silicate minerals on Mars using MRO-CRISM: Geologic context near Nili Fossae and implications for aqueous alteration. *Journal of Geophysical Research*, 114, E00D08. <https://doi.org/10.1029/2009JE003339>
- Elkins-Tanton, L. T., Hess, P. C., & Parmentier, E. M. (2005). Possible formation of ancient crust on Mars through Magma Ocean processes. *Journal of Geophysical Research*, 110(E12), E12S01. <https://doi.org/10.1029/2005JE002480>
- Elkins-Tanton, L. T., Parmentier, E. M., & Hess, P. C. (2003). Magma ocean fractional crystallization and cumulate overturn in terrestrial planets: Implications for Mars. *Meteoritics & Planetary Sciences*, 38(12), 1753–1771. <https://doi.org/10.1111/j.1945-5100.2003.tb00013.x>
- Fassett, C. I., Head, J. W., Smith, D. E., Zuber, M. T., & Neumann, G. A. (2011). Thickness of proximal ejecta from the Orientale basin from Lunar Orbiter Laser Altimeter (LOLA) data: Implications for multi-ring basin formation. *Geophysical Research Letters*, 38(17), L17201. <https://doi.org/10.1029/2011GL048502>
- Filiberto, J. (2017). Geochemistry of Martian basalts with constraints on magma Genesis. *Chemical Geology*, 466, 1–14. <https://doi.org/10.1016/j.chemgeo.2017.06.009>
- Foley, C. N., Economou, T., & Clayton, R. N. (2003). Final chemical results from the Mars Pathfinder alpha proton x-ray spectrometer. *Journal of Geophysical Research*, 108(E12), 8096. <https://doi.org/10.1029/2002JE002019>
- Folkner, W. M., Dehant, V., Maistre, S. L., Yseboodt, M., Rivoldini, A., Hoolst, T. V., et al. (2018). The rotation and interior structure experiment on the insight mission to Mars. *Space Science Reviews*, 214(5), 100. <https://doi.org/10.1007/s11214-018-0530-5>
- Genova, A., Goossens, S., Lemoine, F. G., Mazarico, E., Neumann, G. A., Smith, D. E., & Zuber, M. T. (2016). Seasonal and static gravity field of Mars from MGS, Mars Odyssey and MRO radio science. *Icarus*, 272, 228–245. <https://doi.org/10.1016/j.icarus.2016.02.050>
- Giardini, D., Lognonné, P., Banerdt, W. B., Pike, W. T., Christensen, U., Ceylan, S., et al. (2021). The seismicity of Mars. *Nature Geoscience*, 13(3), 205–212. <https://doi.org/10.1038/s41561-020-0539-8>
- Golombek, M., Grott, M., Kargl, G., Andrade, J., Marshall, J., Warner, N., et al. (2018). Geology and physical properties investigations by the InSight lander. *Space Science Reviews*, 214(5), 84. <https://doi.org/10.1007/s11214-018-0512-7>
- Golombek, M., Kipp, D., Warner, N., Daubar, I. J., Ferguson, R., Kirk, R. L., et al. (2017). Selection of the insight landing site. *Space Science Reviews*, 211(1–4), 5–95. <https://doi.org/10.1007/s11214-016-0321-9>
- Gong, S., & Wieczorek, M. (2021). Depth of Martian magnetization from localized power spectrum analysis. *Journal of Geophysical Research: Planets*, 126(8), e2020JE006690. <https://doi.org/10.1029/2020JE006690>
- Goossens, S., Sabaka, T. J., Genova, A., Mazarico, E., Nicholas, J. B., & Neumann, G. A. (2017). Evidence for a low bulk crustal density for Mars from gravity and topography. *Geophysical Research Letters*, 44(15), 7686–7694. <https://doi.org/10.1002/2017GL074172>
- Guest, A., & Smrekar, S. E. (2005). Relaxation of Martian dichotomy boundary: Faulting in the Ismenius region and constraints on the early evolution of Mars. *Journal of Geophysical Research*, 110(E12), E12S25. <https://doi.org/10.1029/2005JE002504>
- Gyalay, S., Nimmo, F., Plesa, A., & Wieczorek, M. (2020). Constraints on thermal history of Mars from depth of pore closure below InSight. *Geophysical Research Letters*, 47(16), e2020GL088653. <https://doi.org/10.1029/2020GL088653>
- Hahn, B. C., McLennan, S. M., & Klein, E. C. (2011). Martian surface heat production and crustal heat flow from Mars Odyssey gamma-ray spectrometry. *Geophysical Research Letters*, 38(14), L14203. <https://doi.org/10.1029/2011GL047435>

- Head, J. N., Melosh, H. J., & Ivanov, B. A. (2002). Martian meteorite launch: High-speed ejecta from small craters. *Science*, 298(5599), 1752–1756. <https://doi.org/10.1126/science.1077483>
- Heap, M. J. (2019). P- and s-wave velocity of dry, water-saturated, and frozen basalt: Implications for the interpretation of Martian seismic data. *Icarus*, 330, 11–15. <https://doi.org/10.1016/j.icarus.2019.04.020>
- Hobiger, M., Hallo, M., Schmelzbach, C., Stähler, S. C., Fäh, D., Giardini, D., et al. (2021). The shallow structure of Mars at the InSight landing site from inversion of ambient vibrations. *Nature Communications*, 12(1), 6756. <https://doi.org/10.1038/s41467-021-26957-7>
- Hollocher, K. (2022). NORM4 Excel spreadsheet programs to calculate petrologic norms from whole-rock chemical analyses. Version 4. *Zenodo*. <https://doi.org/10.5281/zenodo.5818037>
- Humayun, M., Nemchin, A., Zanda, B., Hewins, R. H., Grange, M., Kennedy, A., et al. (2013). Origin and age of the earliest Martian crust from meteorite NWA 7533. *Nature*, 503(7477), 513–516. <https://doi.org/10.1038/nature12764>
- Ivanov, M., Hiesinger, H., Erkeling, G., Hielscher, F., & Reiss, D. (2012). Major episodes of geologic history of Isidis Planitia on Mars. *Icarus*, 218(1), 24–46. <https://doi.org/10.1016/j.icarus.2011.11.029>
- Kahan, D. S., Folkner, W. M., Buccino, D. R., Dehant, V., Maistre, S. L., Rivoldini, A., et al. (2021). Mars precession rate determined from radiometric tracking of the InSight lander. *Planetary and Space Science*, 199, 105208. <https://doi.org/10.1016/j.pss.2021.105208>
- Karakostas, F., Schmerr, N., Maguire, R., Huang, Q., Kim, D., Lekic, V., et al. (2021). Scattering attenuation of the Martian interior through coda-wave analysis. *Bulletin of the Seismological Society of America*, 111(6), 3035–3054. <https://doi.org/10.1785/0120210253>
- Khan, A., Ceylan, S., Driel, M., Giardini, D., Lognonné, P., Samuel, H., et al. (2021). Upper mantle structure of Mars from InSight seismic data. *Science*, 373(6553), 434–438. <https://doi.org/10.1126/science.abf2966>
- Khan, A., Liebske, C., Rozel, A., Rivoldini, A., Nimmo, F., Connolly, J. A. D., et al. (2018). A geophysical perspective on the bulk composition of Mars. *Journal of Geophysical Research: Planets*, 123(2), 575–611. <https://doi.org/10.1002/2017JE005371>
- Khan, A., Sossi, P. A., Liebske, C., Rivoldini, A., & Giardini, D. (2022). Geophysical and cosmochemical evidence for a volatile-rich Mars. *Earth and Planetary Science Letters*, 578, 117330. <https://doi.org/10.1016/j.epsl.2021.117330>
- Khan, A., van Driel, M., Böse, M., Giardini, D., Ceylan, S., Yan, J., et al. (2016). Single-station and single-event marsquake location and inversion for structure using synthetic Martian waveforms. *Physics of the Earth and Planetary Interiors*, 258, 28–42. <https://doi.org/10.1016/j.pepi.2016.05.017>
- Kim, D., Davis, P., Lekic, V., Maguire, R., Compaire, N., Schimmel, M., et al. (2021). Potential pitfalls in the analysis and structural interpretation of seismic data from the Mars InSight mission. *Bulletin of the Seismological Society of America*, 111(6), 2982–3002. <https://doi.org/10.1785/0120210123>
- Kim, D., Lekic, V., Irving, J. C. E., Schmerr, N., Knapmeyer-Endrun, B., Joshi, R., et al. (2021). Improving constraints on planetary interiors with PPs receiver functions. *Journal of Geophysical Research: Planets*, 126(11), e2021JE006983. <https://doi.org/10.1029/2021JE006983>
- Knapmeyer-Endrun, B., Panning, M. P., Bissig, F., Joshi, R., Khan, A., Kim, D., et al. (2021). Thickness and structure of the Martian crust from InSight seismic data. *Science*, 373(6553), 438–443. <https://doi.org/10.1126/science.abf8966>
- Koepfel, A. H. D., Black, B. A., & Marchi, S. (2019). Differentiation in impact melt sheets as a mechanism to produce evolved magmas on Mars. *Icarus*, 335, 113422. <https://doi.org/10.1016/j.icarus.2019.113422>
- Konopliv, A. S., Park, R. S., Rivoldini, A., Baland, R.-M., Maistre, S. L., Hoolst, T. V., et al. (2020). Detection of the Chandler wobble of Mars from orbiting spacecraft. *Geophysical Research Letters*, 47(21), e2020GL090568. <https://doi.org/10.1029/2020GL090568>
- Kruijer, T. S., Kleine, T., Borg, L. E., Brennecka, G. A., Irving, A. J., Bischoff, A., & Agee, C. B. (2017). The early differentiation of Mars inferred from Hf–W chronometry. *Earth and Planetary Science Letters*, 474, 345–354. <https://doi.org/10.1016/j.epsl.2017.06.047>
- Lapen, T. J., Righter, M., Brandon, A. D., Debaille, V., Beard, B. L., Shafer, J. T., & Peslier, A. H. (2010). A younger age for ALH84001 and its geochemical link to Shergottite sources in Mars. *Science*, 328(5976), 347–351. <https://doi.org/10.1126/science.1185395>
- Lewis, K. W., Peters, S., Gontter, K., Morrison, S., Schmerr, N., Vasavada, A. R., & Gabriel, E. (2019). A surface gravity traverse on Mars indicates low bedrock density at gale crater. *Science*, 363(6426), 535–537. <https://doi.org/10.1126/science.aat0738>
- Lognonné, P., & Johnson, C. (2015). Planetary seismology. In T. Spohn & G. Schubert (Eds.), *Treatise on geophysics* (2nd ed.) (Vol. 10, pp. 65–120). Elsevier-Pergamon. <https://doi.org/10.1016/B978-0-444-53802-4.00167-6>
- Lognonné, P., Banerdt, W. B., Giardini, D., Pike, W. T., Christensen, U., Laudet, P., et al. (2019). Seis: InSight's seismic experiment for internal structure of Mars. *Space Science Reviews*, 215(1), 12. <https://doi.org/10.1007/s11214-018-0574-6>
- Lognonné, P., Banerdt, W. B., Pike, W. T., Giardini, D., Christensen, U., Garcia, R. F., et al. (2020). Constraints on the shallow elastic and anelastic structure of Mars from InSight seismic data. *Nature Geoscience*, 13(3), 213–220. <https://doi.org/10.1038/s41561-020-0536-y>
- Mancinelli, P., Mondini, A. C., Pauselli, C., & Federico, C. (2015). Impact and admittance modeling of the Isidis planitia, Mars. *Planetary and Space Science*, 117, 73–81. <https://doi.org/10.1016/j.pss.2015.04.019>
- Manga, M., & Wright, V. (2021). No cryosphere-confined aquifer below InSight on Mars. *Geophysical Research Letters*, 48(8), e2021GL093127. <https://doi.org/10.1029/2021GL093127>
- Marinova, M. M., Aharonson, O., & Asphaug, E. (2008). Mega-impact formation of the Mars hemispheric dichotomy. *Nature*, 453(7199), 1216–1219. <https://doi.org/10.1038/nature07070>
- Marinova, M. M., Aharonson, O., & Asphaug, E. (2011). Geophysical consequences of planetary-scale impacts into a Mars-like planet. *Icarus*, 211(2), 960–985. <https://doi.org/10.1016/j.icarus.2010.10.032>
- Martin, B., & Fyfe, W. S. (1970). Some experimental and theoretical observations on the kinetics of hydration reactions with particular reference to serpentinization. *Chemical Geology*, 6, 185–202. [https://doi.org/10.1016/0009-2541\(70\)90018-5](https://doi.org/10.1016/0009-2541(70)90018-5)
- McCubbin, F. M., Boyce, J. W., Novák-Szabó, T., Santos, A. R., Tartèse, R., Muttik, N., et al. (2016). Geologic history of Martian regolith breccia Northwest Africa 7034: Evidence for hydrothermal activity and lithologic diversity in the Martian crust. *Journal of Geophysical Research: Planets*, 121(10), 2120–2149. <https://doi.org/10.1002/2016JE005143>
- McCubbin, F. M., Nekvasil, H., Harrington, A. D., Elardo, S. M., & Lindsley, D. H. (2008). Compositional diversity and stratification of the Martian crust: Inferences from crystallization experiments on the picrobasalt Humphrey from Gusev Crater, Mars. *Journal of Geophysical Research*, 113(E11), E11013. <https://doi.org/10.1029/2008JE003165>
- McGovern, P. J., Solomon, S. C., Smith, D. E., Zuber, M. T., Simons, M., Wiczorek, M. A., et al. (2002). Localized gravity/topography admittance and correlation spectra on Mars: Implications for regional and global evolution. *Journal of Geophysical Research*, 107(E12), 19-1–19-25. <https://doi.org/10.1029/2002JE001854>
- McGovern, P. J., Solomon, S. C., Smith, D. E., Zuber, M. T., Simons, M., Wiczorek, M. A., & Head, J. W. (2004). Correction to “Localized gravity/topography admittance and correlation spectra on Mars: Implications for regional and global evolution”. *Journal of Geophysical Research*, 109(E7), E07007. <https://doi.org/10.1029/2004JE002286>
- McLennan, S. M. (2001). Crustal heat production and the thermal evolution of Mars. *Geophysical Research Letters*, 28(21), 4019–4022. <https://doi.org/10.1029/2001GL013743>

- McLennan, S. M. (2003). Large-ion lithophile element fractionation during the early differentiation of Mars and the composition of the Martian primitive mantle. *Meteoritics & Planetary Sciences*, 38(6), 895–904. <https://doi.org/10.1111/j.1945-5100.2003.tb00286.x>
- McLennan, S. M. (2022). Composition of planetary crusts and planetary differentiation. In T. K. P. Gregg, R. M. C. Lopes, & S. A. Fagents (Eds.), *Planetary volcanism across the solar system* (pp. 287–331). Elsevier. <https://doi.org/10.1016/B978-0-12-813987-5.00008-0>
- McSween, H., & McLennan, S. (2014). Mars. In H. D. Holland & K. K. Turekian (Eds.), *Treatise on geochemistry* (2nd ed., pp. 251–300). Elsevier. <https://doi.org/10.1016/B978-0-08-095975-7.00125-X>
- McSween, H. Y., Jr, Taylor, G. J., & Wyatt, M. B. (2009). Elemental composition of the Martian crust. *Science*, 324(5928), 736–739. <https://doi.org/10.1126/science.1165871>
- Menina, S., Margerin, L., Kawamura, T., Lognonné, P., Marti, J., Drilleau, M., et al. (2021). Energy envelope and attenuation characteristics of high-frequency (HF) and very-high-frequency (VF) Martian events. *Bulletin of the Seismological Society of America*, 111(6), 3016–3034. <https://doi.org/10.1785/0120210127>
- Michalski, J. R., Niles, P. B., Glotch, T. D., & Cuadros, J. (2021). Infrared spectral evidence for K-metasomatism of volcanic rocks on Mars. *Geophysical Research Letters*, 48(10), e2021GL093882. <https://doi.org/10.1029/2021GL093882>
- Milbury, C., Johnson, B. C., Melosh, H. J., Collins, G. S., Blair, D. M., Soderblom, J. M., et al. (2015). Preimpact porosity controls the gravity signature of lunar craters. *Geophysical Research Letters*, 42(22), 9711–9716. <https://doi.org/10.1002/2015GL066198>
- Miljković, K., Wieczorek, M. A., Collins, G. S., Solomon, S. C., Smith, D. E., & Zuber, M. T. (2015). Excavation of the lunar mantle by basin-forming impact events on the Moon. *Earth and Planetary Science Letters*, 409, 243–251. <https://doi.org/10.1016/j.epsl.2014.10.041>
- Mittelholz, A., Johnson, C. L., Feinberg, J. M., Langlais, B., & Phillips, R. J. (2020). Timing of the Martian dynamo: New constraints for a core field 4.5 and 3.7 Ga ago. *Science Advances*, 6(18), eaba0513. <https://doi.org/10.1126/sciadv.aba0513>
- Mohorovičić, A. (1992). Earthquake of 8 October 1909 (translation in English). *Geofizika*, 9, 3–55.
- Moody, J. B. (1976). Serpentinization: A review. *Lithos*, 9(2), 125–138. [https://doi.org/10.1016/0024-4937\(76\)90030-X](https://doi.org/10.1016/0024-4937(76)90030-X)
- Mustard, J. F., Poulet, F., Gendrin, A., Bibring, J.-P., Langevin, Y., Gondet, B., et al. (2005). Olivine and pyroxene diversity in the crust of Mars. *Science*, 307(5715), 1594–1597. <https://doi.org/10.1126/science.1109098>
- Nakamura, Y., & Anderson, D. L. (1979). Martian wind activity detected by a seismometer at Viking lander 2 site. *Geophysical Research Letters*, 6, 499–502. <https://doi.org/10.1029/GL006i006p00499>
- Neumann, G. A., Zuber, M. T., Wieczorek, M. A., McGovern, P. J., Lemoine, F. G., & Smith, D. E. (2004). Crustal structure of Mars from gravity and topography. *Journal of Geophysical Research*, 109(E8), E08002. <https://doi.org/10.1029/2004JE002262>
- Nimmo, F. (2002). Admittance estimates of mean crustal thickness and density at the Martian hemispheric dichotomy. *Journal of Geophysical Research*, 107(E11), 5117. <https://doi.org/10.1029/2000JE001488>
- Nimmo, F., Hart, S. D., Korycansky, D. G., & Agnor, C. B. (2008). Implications of an impact origin for the Martian hemispheric dichotomy. *Nature*, 453(7199), 1220–1223. <https://doi.org/10.1038/nature07025>
- Nimmo, F., & Stevenson, D. J. (2001). Estimates of Martian crustal thickness from viscous relaxation of topography. *Journal of Geophysical Research*, 106(E3), 5085–5098. <https://doi.org/10.1029/2000JE001331>
- Nimmo, F., & Tanaka, K. (2005). Earth crustal evolution of Mars. *Annual Review of Earth and Planetary Sciences*, 33(1), 133–161. <https://doi.org/10.1146/annurev.earth.33.092203.122637>
- Norman, M. D. (1999). The composition and thickness of the crust of Mars estimated from rare Earth elements and neodymium-isotopic compositions of Martian meteorites. *Meteoritics & Planetary Sciences*, 34(3), 439–449. <https://doi.org/10.1111/j.1945-5100.1999.tb01352.x>
- Nyquist, L. E., Shih, C.-Y., McCubbin, F. M., Santos, A. R., Shearer, C. K., Peng, Z. X., et al. (2016). Rb-Sr and Sm-Nd isotopic and REE studies of igneous components in the bulk matrix domain of Martian breccia Northwest Africa 7034. *Meteoritics & Planetary Sciences*, 51(3), 483–498. <https://doi.org/10.1111/maps.12606>
- Ojha, L., Karimi, S., Buffo, J., Nerozzi, S., Holt, J. W., Smrekar, S., & Chevrier, V. (2021). Martian mantle heat flow estimate from the lack of lithospheric flexure in the south pole of Mars: Implications for planetary evolution and basal melting. *Geophysical Research Letters*, 48(2), e2020GL091409. <https://doi.org/10.1029/2020GL091409>
- Ojha, L., Karimi, S., Lewis, K. W., Smrekar, S. E., & Siegler, M. (2019). Depletion of heat producing elements in the Martian mantle. *Geophysical Research Letters*, 46(22), 12756–12763. <https://doi.org/10.1029/2019GL085234>
- Ojha, L., & Lewis, K. (2018). The density of the Medusae Fossae formation: Implications for its composition, origin, and importance in Martian history. *Journal of Geophysical Research: Planets*, 123(6), 1368–1379. <https://doi.org/10.1029/2018JE005565>
- Pan, C., Rogers, A. D., & Michalski, J. R. (2015). Thermal and near-infrared analyses of central peaks of Martian impact craters: Evidence for a heterogeneous Martian crust. *Journal of Geophysical Research: Planets*, 120(4), 662–688. <https://doi.org/10.1002/2014JE004676>
- Pan, L., Quantin-Nataf, C., Tauzin, B., Michaut, C., Golombek, M., Lognonné, P., et al. (2020). Crust stratigraphy and heterogeneities of the first kilometers at the dichotomy boundary in Western Elysium Planitia and implications for InSight lander. *Icarus*, 338, 113511. <https://doi.org/10.1016/j.icarus.2019.113511>
- Panning, M. P., Beucler, E., Drilleau, M., Mocquet, A., Lognonné, P., & Banerdt, W. B. (2015). Verifying single-station seismic approaches using Earth-based data: Preparation for data return from the InSight mission to Mars. *Icarus*, 248, 230–242. <https://doi.org/10.1016/j.icarus.2014.10.035>
- Parro, L. M., Jiménez-Díaz, A., Mansilla, F., & Ruiz, J. (2017). Present-day heat flow model of Mars. *Scientific Reports*, 7(1), 45629. <https://doi.org/10.1038/srep45629>
- Pauer, M., & Breuer, D. (2008). Constraints on the maximum crustal density from gravity–topography modeling: Applications to the southern highlands of Mars. *Earth and Planetary Science Letters*, 276(3–4), 253–261. <https://doi.org/10.1016/j.epsl.2008.09.014>
- Plesa, A.-C., Grott, M., Tosi, N., Breuer, D., Spohn, T., & Wieczorek, M. A. (2016). How large are present-day heat flux variations across the surface of Mars? *Journal of Geophysical Research: Planets*, 121(12), 2386–2403. <https://doi.org/10.1002/2016JE005126>
- Plesa, A.-C., Padovan, S., Tosi, N., Breuer, D., Grott, M., Wieczorek, M. A., et al. (2018). The thermal state and interior structure of Mars. *Geophysical Research Letters*, 45(22), 12198–12209. <https://doi.org/10.1029/2018GL080728>
- Poulet, F., Mangold, N., Platevoet, B., Bardintzeff, J.-M., Sautter, V., Mustard, J., et al. (2009). Quantitative compositional analysis of Martian mafic regions using the MEx/OMEGA reflectance data. 2. Petrological implications. *Icarus*, 201(1), 84–101. <https://doi.org/10.1016/j.icarus.2008.12.042>
- Quesnel, Y., Sotin, C., Langlais, B., Costin, S., Mandea, M., Gottschalk, M., & Dymant, J. (2009). Serpentinization of the Martian crust during Noachian. *Earth and Planetary Science Letters*, 277(1–2), 184–193. <https://doi.org/10.1016/j.epsl.2008.10.012>
- Rae, A. P., Collins, G. S., Morgan, J. V., Salge, T., Christeson, G. L., Leung, J., et al. (2019). Impact induced porosity and microfracturing at the Chicxulub impact structure. *Journal of Geophysical Research: Planets*, 124(7), 1960–1978. <https://doi.org/10.1029/2019JE005929>
- Ritzer, J. A., & Hauck, S. A., II. (2009). Lithospheric structure and tectonics at Isidis planitia, Mars. *Icarus*, 201(2), 528–539. <https://doi.org/10.1016/j.icarus.2009.01.025>

- Rivoldini, A., Hoolst, T. V., Verhoeven, O., Mocquet, A., & Dehant, V. (2011). Geodesy constraints on the interior structure and composition of Mars. *Icarus*, 213(2), 451–472. <https://doi.org/10.1016/j.icarus.2011.03.024>
- Rogers, A. D., & Nekvasil, H. (2015). Feldspathic rocks on Mars: Compositional constraints from infrared spectroscopy and possible formation mechanisms. *Geophysical Research Letters*, 42(8), 2619–2626. <https://doi.org/10.1002/2015GL063501>
- Rychert, C. A., & Shearer, P. M. (2010). Resolving crustal thickness using SS waveform stacks. *Geophysical Journal International*, 180(3), 1128–1137. <https://doi.org/10.1111/j.1365-246X.2009.04497.x>
- Santos, A. R., Agee, C. B., McCubbin, F. M., Shearer, C. K., Burger, P. V., Tartèse, R., & Anand, M. (2015). Petrology of igneous clasts in Northwest Africa 7034: Implications for the petrologic diversity of the Martian crust. *Geochimica et Cosmochimica Acta*, 157, 56–85. <https://doi.org/10.1016/j.gca.2015.02.023>
- Sautter, V., & Payre, V. (2021). Alkali magmatism on Mars: An unexpected diversity. *Comptes Rendus Geoscience*, 353(S2), 1–30. <https://doi.org/10.5802/crgeos.64>
- Sautter, V., Toplis, M. J., Beck, P., Mangold, N., Wiens, R., Pinet, P., et al. (2016). Magmatic complexity on early Mars as seen through a combination of orbital, in-situ and meteorite data. *Lithos*, 254–255, 36–52. <https://doi.org/10.1016/j.lithos.2016.02.023>
- Sautter, V., Toplis, M. J., Wiens, R. C., Cousin, A., Fabre, C., Gasnault, O., et al. (2015). In situ evidence for continental crust on early Mars. *Nature Geoscience*, 8, 605–609. <https://doi.org/10.1038/NNGEO2474>
- Schmidt, M. E., Campbell, J. L., Gellert, R., Perrett, G. M., Treiman, A. H., Blaney, D. L., et al. (2014). Geochemical diversity in first rocks examined by the Curiosity Rover in Gale Crater: Evidence for an alkali and volatile-rich igneous source. *Journal of Geophysical Research: Planets*, 119(1), 64–81. <https://doi.org/10.1002/2013JE004481>
- Searls, M. L., Banerdt, W. B., & Phillips, R. J. (2006). Utopia and Hellas basins, Mars: Twins separated at birth. *Journal of Geophysical Research*, 111(E8), E08005. <https://doi.org/10.1029/2005JE002666>
- Smith, M. R., & Bandfield, J. L. (2012). Geology of quartz and hydrated silica-bearing deposits near Antoniadi crater, Mars. *Journal of Geophysical Research*, 117(E6), E06007. <https://doi.org/10.1029/2011JE004038>
- Smrekar, S., Lognonné, P., Spohn, T., Banerdt, B., Breuer, D., Christensen, U., et al. (2019). Pre-mission InSights on the interior of Mars. *Space Science Reviews*, 215(1), 3. <https://doi.org/10.1007/s11214-018-0563-9>
- Sohl, F., Schubert, G., & Spohn, T. (2005). Geophysical constraints on the composition and structure of the Martian interior. *Journal of Geophysical Research*, 110(E12), E12008. <https://doi.org/10.1029/2005JE002520>
- Spudis, P. D. (1993). *The geology of multi-ring impact basins*. Cambridge University Press.
- Stähler, S. C., Khan, A., Banerdt, W. B., Lognonné, P., Giardini, D., Ceylan, S., et al. (2021). Seismic detection of the Martian core. *Science*, 373(6553), 443–448. <https://doi.org/10.1126/science.abi7730>
- Stolper, E. M., Baker, M. B., Newcombe, M. E., Schmidt, M. E., Treiman, A. H., Cousin, A., et al. (2013). The petrochemistry of Jake_M: A martian mugearite. *Science*, 341(6153), 1239463. <https://doi.org/10.1126/science.1239463>
- Tanaka, K. L., Skinner, J. A., Jr, Dohm, J. M., Irwin, R. P., III, Kolb, E. J., Fortezzo, C. M., et al. (2014). Geologic map of Mars. *U.S. Geological Survey, Scientific Investigations Map*, 3292. scale 1:20,000,000. <https://doi.org/10.3133/sim3292>
- Taylor, G. J., Boynton, W., Brückner, J., Wänke, H., Dreibus, G., Kerry, K., et al. (2006). Bulk composition and early differentiation of Mars. *Journal of Geophysical Research*, 111(E3), 3. <https://doi.org/10.1029/2005JE002645>
- Taylor, S. R., & McLennan, S. M. (2009). *Planetary crusts: Their composition, origin and evolution*. Cambridge University Press.
- Tenzer, R., Eshagh, M., & Jin, S. (2015). Martian sub-crustal stress from gravity and topographic models. *Earth and Planetary Science Letters*, 425, 84–92. <https://doi.org/10.1016/j.epsl.2015.05.049>
- Thiriet, M., Michaut, C., Breuer, D., & Plesa, A.-C. (2018). Hemispheric dichotomy in lithosphere thickness on Mars caused by differences in crustal structure and composition. *Journal of Geophysical Research*, 123(4), 823–848. <https://doi.org/10.1002/2017JE005431>
- Toft, P. B., Arkani-Hamed, J., & Haggerty, S. E. (2009). The effects of serpentinization on density and magnetic susceptibility: A petrophysical model. *Physics of the Earth and Planetary Interiors*, 65(1–2), 137–157. [https://doi.org/10.1016/0031-9201\(90\)90082-9](https://doi.org/10.1016/0031-9201(90)90082-9)
- Udry, A., Gazel, E., & McSween, H. Y., Jr. (2018). Formation of evolved rocks at Gale crater by crystal fractionation and implications for Mars crustal composition. *Journal of Geophysical Research: Planets*, 123(6), 1525–1540. <https://doi.org/10.1029/2018JE005602>
- Udry, A., Howarth, G. H., Herd, C. D. K., Day, J. M. D., Lapen, T. J., & Filiberto, J. (2020). What Martian meteorites reveal about the interior and surface of Mars. *Journal of Geophysical Research: Planets*, 125(12), e2020JE006523. <https://doi.org/10.1029/2020JE006523>
- van der Meijde, M., Fadel, I., Ditmar, P., & Hamayun, M. (2015). Uncertainties in crustal thickness models for data sparse environments: A review for south America and Africa. *Journal of Geodynamics*, 84, 1–18. <https://doi.org/10.1016/j.jog.2014.09.013>
- Vaughan, W. M., & Head, J. W. (2014). Impact melt differentiation in the South Pole-Aitken basin: Some observations and speculations. *Planetary and Space Science*, 91, 101–106. <https://doi.org/10.1016/j.pss.2013.11.010>
- Vaughan, W. M., Head, J. W., Wilson, L., & Hess, P. C. (2013). Geology and petrology of enormous volumes of impact melt on the Moon: A case study of the Orientale basin impact melt sea. *Icarus*, 223(2), 749–765. <https://doi.org/10.1016/j.icarus.2013.01.017>
- Wahl, D., Wiczeorek, M. A., Wünnemann, K., & Oberst, J. (2020). Crustal porosity of lunar impact basins. *Journal of Geophysical Research: Planets*, 125(4), e2019JE006335. <https://doi.org/10.1029/2019JE006335>
- Warner, N. H., Golombek, M. P., Sweeney, J., Ferguson, R., Kirk, R., & Schwartz, C. (2017). Near surface stratigraphy and regolith production in southwestern Elysium Planitia, Mars: Implications for Hesperian-Amazonian terrains and the InSight lander mission. *Space Science Reviews*, 211(1–4), 147–190. <https://doi.org/10.1007/s11214-017-0352-x>
- Watts, A. B. (2001). *Isostasy and flexure of the lithosphere*. Cambridge University Press.
- Werner, S. C. (2008). The early Martian evolution—Constraints from basin formation ages. *Icarus*, 195(1), 45–60. <https://doi.org/10.1016/j.icarus.2007.12.008>
- Wiczeorek, M. A. (2022). Insight crustal thickness archive [Data Set]. Zenodo. <https://doi.org/10.5281/zenodo.6477509>
- Wiczeorek, M. A. (2015). Gravity and topography of the terrestrial planets. In T. Spohn & G. Schubert (Eds.) *Treatise on geophysics* (2nd ed.) (Vol. 10, pp. 153–193). Elsevier-Pergamon. <https://doi.org/10.1016/B978-0-444-53802-4.00169-X>
- Wiczeorek, M. A. (2021). *Ctplanet*. version 0.2.1 (Vol. 0.2.1). Zenodo. <https://doi.org/10.5281/zenodo.4439426>
- Wiczeorek, M. A., Beuthe, M., Rivoldini, A., & Hoolst, T. V. (2019). Hydrostatic interfaces in bodies with nonhydrostatic lithospheres. *Journal of Geophysical Research: Planets*, 124, 1410–1432. <https://doi.org/10.1029/2018JE005909>
- Wiczeorek, M. A., & Meschede, M. (2018). SHTools: Tools for working with spherical harmonics. *Geochemistry, Geophysics, Geosystems*, 19(8), 2574–2592. <https://doi.org/10.1029/2018GC007529>
- Wiczeorek, M. A., Neumann, G. A., Nimmo, F., Kiefer, W. S., Taylor, G. J., Melosh, H. J., et al. (2013). The crust of the Moon as seen by GRAIL. *Science*, 339(6120), 671–675. <https://doi.org/10.1126/science.1231530>
- Wiczeorek, M. A., & Phillips, R. J. (1998). Potential anomalies on a sphere: Applications to the thickness of the lunar crust. *Journal of Geophysical Research*, 103(E1), 1715–1724. <https://doi.org/10.1029/97JE03136>

- Wieczorek, M. A., & Zuber, M. T. (2004). Thickness of the Martian crust: Improved constraints from geoid-to-topography ratios. *Journal of Geophysical Research*, *109*(E1), E01009. <https://doi.org/10.1029/2003JE002153>
- Wray, J. J., Hansen, S. T., Dufek, J., Swayze, G. A., Murchie, S. L., Seelos, F. P., et al. (2013). Prolonged magmatic activity on Mars inferred from the detection of felsic rocks. *Nature Geoscience*, *6*(12), 1013–1017. <https://doi.org/10.1038/NGEO1994>
- Zuber, M. T., Solomon, S. C., Phillips, R. J., Smith, D. E., Tyler, G. L., Aharonson, O., et al. (2000). Internal structure and early thermal evolution of Mars from Mars Global Surveyor topography and gravity. *Science*, *287*(5459), 1788–1793. <https://doi.org/10.1126/science.287.5459.1788>